Received: 19 April 2021 | Revised: 29 July 2021 | Accepted: 29 August 2021

DOI: 10.1002/suco.202100257

ARTICLE

fib CEB-FIP WILEY

Time-dependent cyclic behavior of reinforced concrete bridge columns under chlorides-induced corrosion and rebars buckling

Angelo Pelle[1] | **Bruno Briseghella**[2] | **Alessandro Vittorio Bergami**[1] | **Gabriele Fiorentino**[3] | **Gian Felice Giaccu**[4] | **Davide Lavorato**[1] | **Giuseppe Quaranta**[5] | **Alessandro Rasulo**[6] | **Camillo Nuti**[1]

[1]Department of Architecture, Roma Tre University, Rome, Italy

[2]College of Civil Engineering, Fuzhou University, Fuzhou, China

[3]Department of Civil Engineering, University of Bristol, Bristol, UK

[4]Department of Architecture, Design and Urban Planning, University of Sassari, Alghero, Italy

[5]Department of Structural and Geotechnical Engineering, Sapienza University of Rome, Rome, Italy

[6]Department of Civil and Mechanical Engineering, University of Cassino and Southern Lazio, Cassino, Italy

Correspondence
Giuseppe Quaranta, Department of Structural and Geotechnical Engineering, Sapienza University of Rome, Via Eudossiana 18, 00184 Rome, Italy.
Email: giuseppe.quaranta@uniroma1.it

Funding information
Federbeton, Grant/Award Number: "Seismic Behaviour of Integral Bridges"; Laboratories University Network of Seismic Engineering (ReLUIS), Grant/Award Numbers: DPC/ReLUIS 2019-2021 - UR RM1 WP 4-11, DPC/ReLUIS 2019-2021 - UR RM3 WP 11.2-11.3; National Natural Science Foundation of China, Grant/Award Number: 51778148; Sapienza Università di Roma, Grant/Award Number: RM120172B37F0628

Abstract

This study presents the results of a refined numerical investigation meant at understanding the time-dependent cyclic behavior of reinforced concrete (RC) bridge columns under chlorides-induced corrosion. The chloride ingress in the cross-section of the bridge column is simulated, taking into account the effects of temperature, humidity, aging, and corrosion-induced cover cracking. Once the partial differential equations governing such multiphysics problem are solved through the finite-element method, the loss of reinforcement steel bars cross-section is calculated based on the estimated corrosion current density. The nonlinear cyclic response of the RC bridge column under corrosion is, thus, determined by discretizing its cross-sections into several unidirectional fibers. In particular, the nonlinear modeling of the corroded longitudinal rebars exploits a novel proposal for the estimation of the ultimate strain in tension and also accounts for buckling under compression. A parametric numerical study is finally conducted for a real case study to unfold the role of corrosion pattern and buckling mode of the longitudinal rebars on the time variation of capacity and ductility of RC bridge columns.

KEYWORDS

bridge column, chloride, finite-element analysis, generalized corrosion, multiphysics analysis, pitting corrosion, rebar buckling, reinforced concrete, seismic response

1 | INTRODUCTION

The assessment of reinforced concrete (RC) bridges subjected to deterioration phenomena is of utmost importance because of the safety issues that can occur under serviceability loads and/or exceptional events (e.g., earthquakes). Among the possible causes of RC bridges deterioration, corrosion can jeopardize significantly the global structural safety even in a short time window as compared with the design lifetime. The corrosion induced by chlorides transported by sea aerosol close to coastal zones or originated from some industrial activities but also due to the use of deicing salts in mountain regions turns out to be very severe for RC members[1,2] and thus deserves special consideration. Within this framework, a recent statistical study[3] based on a dataset including 20,000 coastal bridges extracted from the National Bridge Inventory of the US Federal Highway Administration has demonstrated that the durability of bridges is noticeably affected by sea chlorides at coastal distances up to 2–3 km inland. Another statistical study[4] based on Monte Carlo simulations also pointed out that if chloride and moisture contents are large enough to initiate the corrosion at inland locations, then the long-term damage risk is likely to increase significantly under climate change. It is evident that resources allocation as well as prioritization of the actions needed for ensuring the minimum safety level of transportation networks call for the long-term assessment of RC bridges under chlorides-induced corrosion. This, in turn, has motivated many valuable studies in recent years.

On the one side, approaches based on multiphysics analysis have been pursed to evaluate the evolution in time of the structural capacity. For instance, Alipour et al.[5,6] performed a multiphysics-based simulation of the chloride ingress into concrete under the assumption that the process is dominated by diffusion phenomenon by taking into account the effects due to temperature, humidity, and concrete aging. A set of multi-span regular RC bridges has been investigated through numerical simulations. The deck is modeled using linear-elastic elements while the columns are modeled using inelastic beam-column elements, where the plasticity has been concentrated over a specified length of element ends. Nonlinear dynamic analyses have been presented to evaluate the evolution in time of the deck drift ratio, and fragility analyses have been performed, considering the column curvature ductility as damage measure. Furthermore, the moment-curvature response of the bridge columns has been discussed together with the results of standard nonlinear static (pushover) analysis. More recently, Zhou et al.[7] analyzed an existing RC arch bridge. In that study, the chloride ingress is simulated as a diffusion process, and the multiphysics analysis herein reported accounts for the influence of the temperature only. The numerical assessment of corroded RC members has been evaluated against static actions due to self-weight and traffic loading.

Other studies have focused on the accurate numerical modeling of corroded RC bridge components. For instance, Kashani et al.[8,9] developed, calibrated, and tested a phenomenological uniaxial material model for corroded reinforcing steel bars in RC bridge columns that account for the effect of inelastic buckling and low-cycle fatigue. Recently, Rasulo et al.[10] have addressed the analysis of RC bridge columns taking into account flexure–shear interaction. To this end, they considered a fiber-based, nonlinear beam-column finite element with zero-length rotational spring at the ends to simulate the bond-slip behavior and a base zero-length translational spring to account for the shear behavior. The residual capacity of RC grillage decks under static loads has been examined by Conti et al.,[11] who paid special attention on the numerical modeling of its torsional response. Marí et al.[12] analyzed an RC footbridge affected by corrosion at the bottom layer of reinforcement due to exposure to marine environment. The interested reader can refer to a recent state-of-the-art review paper by Kashani et al.[13] for an experimental-based critical discussion about the effects of corrosion on strength and ductility of corroded RC bridge components.

For the sake of completeness, it should be not underestimated the relevance of corrosion scenarios in bridges made of prestressed or posttensioned concrete members. For more information about this topic, the interested reader can refer, for instance, to numerical and experimental studies by Belletti et al.[14,15] A useful review paper dealing with corroded prestressed and posttensioned concrete structures has been completed recently by Vereecken et al.[16]

In this perspective, the present work is targeted at investigating the long-term behavior of RC bridge columns under chlorides-induced corrosion. Initially, the multiphysics simulation of the chloride transport is

detailed. Besides the effects of environmental factors and aging, a simplified approach is here adopted to take into account those due to corrosion-induced cover cracking. Once the corrosion current density is thus calculated, a parametric description of the corrosion pattern is presented. Next, the nonlinear modeling of the RC bridge column is addressed. The final structural model employs a novel proposal for the estimation of the ultimate strain in tension of the corroded longitudinal reinforcing steel bars and also accounts for buckling under compression. Finally, the results obtained for a real case study are discussed extensively to derive useful recommendations.

2 | CHLORIDE INGRESS AND CORROSION CURRENT DENSITY IN RC BRIDGE COLUMNS

A multiphysics FE based analysis is performed to evaluate the chloride concentration within an RC bridge column made of ordinary Portland cement (OPC). This multiphysics simulation of the chloride transport resembles to some extent the ones presented in previous studies[5–7] for the time-dependent assessment of corroded RC bridges. Compared with the previous studies in this field, a simplified, yet effective, approach is also implemented to evaluate the effect of cover cracking due to the reinforcement corrosion on chloride transport. Furthermore, the proposed multiphysics FE based analysis is ultimately completed with the estimate of the corrosion current density given the amount of chloride into concrete together with material properties and environmental conditions. This section is intended to illustrate main assumptions, governing equations, relevant material data, and references adopted to simulate the chloride transport as well as to determine the corrosion current density.

2.1 | Chloride transport modeling

It is known that chloride in concrete can be either dissolved in the pore solution (free chloride) or chemically and physically bound to the cement hydrates (bound chloride). Free chloride dissolved in the pore solution is responsible for initiating the process of corrosion. Transport mechanisms relevant to chloride penetration into concrete include ionic diffusion and capillarity sorption (convection). In agreement with previous studies,[5–7,17–19] it is assumed that chloride ingress in concrete can be effectively approximated as diffusion-like process (on the other hand, it is understood that chloride cannot pass through reinforcing steel bars). Given the 2D domain of the bridge column section defined by the set of coordinates (x,y), according to the Fick's first law of diffusion:

$$J_c = -D_c\left(\frac{\partial C_{fc}}{\partial x}+\frac{\partial C_{fc}}{\partial y}\right), \tag{1}$$

where J_c [kg/(m^{2}s)] is the flux of chloride ions due to diffusion, D_c [m^2/s] is the effective chloride diffusion coefficient, and C_{fc} [kg/m^3 of concrete] is the concentration of chloride dissolved in the pore solution (free chloride). The use of Equation (1) presumes that concrete is an isotropic material with respect to chloride ingress. Given C_{fc} [kg/m^3 of pore solution], Equation (1) is reformulated as follows:

$$J_c = -D_c\omega_e\left(\frac{\partial C_{fc}}{\partial x}+\frac{\partial C_{fc}}{\partial y}\right), \tag{2}$$

where ω_e [m^3 of evaporable water/m^3 of concrete]. It is defined as the water held in both capillary and gel pores.

By imposing the mass conservation law as a function of the time parameter t [s], it is obtained:

$$\frac{\partial C_{tc}}{\partial t} = -\frac{\partial J_{cx}}{\partial x}-\frac{\partial J_{cy}}{\partial y}, \tag{3}$$

where C_{tc} [kg/m^3 of concrete] is the total chloride concentration whereas J_{cx} and J_{cy} [kg/(m^{2}s)] are the flux of chloride ions due to diffusion in the x and y directions, respectively. By introducing Equation (2) into Equation (3), the Fick's second law is obtained:

$$\frac{\partial C_{tc}}{\partial t} = \frac{\partial}{\partial x}\left(D_c\omega_e\frac{\partial C_{fc}}{\partial x}\right)+\frac{\partial}{\partial y}\left(D_c\omega_e\frac{\partial C_\infty}{\partial y}\right). \tag{4}$$

2.1.1 | Chloride binding isotherm

The effect of chloride binding is relevant because: (i) the rate of chloride ionic transport in concrete decreases, because the amount of available mobile ions (free chloride) is reduced and (ii) the reduction of free chloride in concrete results in lower amounts of chloride at the reinforcing steel, thereby causing a delay in the onset of corrosion. It is, thus, appropriate to revise Equation (4), taking into account that:

$$C_{tc} = C_{bc}+\omega_e C_{fc}, \tag{5}$$

where C_{bc} [kg/m^3 of concrete] is the concentration of bound chloride. By applying the mass conservation law

to Equation (5) and substituting into Equation (4), the Fick's second law is reformulated as follows:

$$\frac{\partial C_{fc}}{\partial t}=\frac{\partial}{\partial x}\left(D_c^*\frac{\partial C_{fc}}{\partial x}\right)+\frac{\partial}{\partial y}\left(D_c^*\frac{\partial C_{fc}}{\partial y}\right), \tag{6}$$

where:

$$D_c^*=\frac{D_c}{1+\frac{1}{\omega_e}\frac{\partial C_{bc}}{\partial C_{fc}}}. \tag{7}$$

Herein, D_c^* [m^2/s] is the apparent diffusion coefficient, whereas $\partial C_{bc}/\partial C_{fc}$ is known as binding capacity.

The chloride binding isotherm $C_{bc}(C_{fc})$ must be specified to estimate D_c^* [m^2/s] according to Equation (7). In the present work, the Langmuir isotherm is employed, which reads:

$$C_{bc}=\frac{\alpha_L C_{fc}}{1+\beta_L C_{fc}}\rightarrow\frac{\partial C_{bc}}{\partial C_{fc}}=\frac{\alpha_L}{(1+\beta_L C_{fc})^2}, \tag{8}$$

where α_L [m^3 of pore solution/m^3 of concrete] and β_L [m^3 of pore solution/kg] are given constants. The Langmuir isotherm is here employed by assuming $\alpha_L=0.39$ m^3 of pore solution/m^3 of concrete and $\beta_L=0.07$ m^3 of pore solution/kg in agreement with previous studies.[6,17,18] It is understood that such modeling implies the simplified assumption of an instantaneous equilibrium between C_{fc} and C_{bc}.

2.1.2 | Chloride diffusion coefficient

Several physical, chemical, and mechanical concurrent phenomena have influence on the chloride diffusion. In the present work, D_c in Equation (7) is calculated as follows:

$$D_c=D_{c,ref}F_T(T)F_h(h)F_\delta(\delta)F_t(t), \tag{9}$$

where $D_{c,ref}$ [m^2/s] is the reference chloride diffusion coefficient (i.e., D_c value for reference conditions). The parameters $F_T(T)$ and $F_h(h)$ are the corrective factors of the chloride diffusion coefficient that take into account the effects due to temperature T [K] and pore relative humidity h, respectively. Moreover, the factors $F_\delta(\delta)$ and $F_t(t)$ serve at taking into account the effects of cover crack width δ [mm] and concrete age t [s] on chloride diffusion coefficient, respectively. The parameter $D_{c,ref}$ is assumed to be constant, and its value depends on the concrete composition. In this regard, it will be assumed henceforth a cement content c equal to 400 kg of cement/m^3 of concrete and a water-to-cement ratio w/c equal to 0.5. For the next numerical simulations, it is considered $D_{c,ref}=4.5\cdot10^{-12}$ m^2/s.

In agreement with most of the existing studies,[5–7,17–19] dependence of the chloride diffusivity on temperature is estimated using the Arrhenius law as follows:

$$F_T=\exp\left[\frac{U_c}{R_G}\left(\frac{1}{T_{ref}}-\frac{1}{T}\right)\right], \tag{10}$$

where U_c [kJ/mol] is the activation energy of the chloride diffusion process, $R_G=8.314\cdot10^{-3}$ kJ/(Kmol) is the gas constant, and $T_{ref}=296.15$ K is the constant reference temperature. For $w/c=0.5$, it can be assumed $U_c=44.6$ kJ/mol.

It is rather common in the existing literature to also account for the effects of the pore relative humidity h through the following corrective factor[5,6,17–19]:

$$F_h=\left[1+\left(\frac{1-h}{1-h_c}\right)^4\right]^{-1}, \tag{11}$$

where h_c is the value of h at which D_c drops halfway between its highest and lowest value. Its values are typically constant and equal to 0.75.

For the sake of simplicity, Fick's second law is often used for estimating the chloride penetration into concrete even when cracks are present, and, in agreement with this assumption, many experimental studies have been performed to evaluate the corresponding amplification factor for the reference chloride diffusion coefficient.[20,21] For a concrete composition very similar to that considered in the present study, Shao-feng et al.[21] derived experimentally the following relationship:

$$F_\delta=\max\left\{1,47.18\delta^2-8.18\delta+1\right\}. \tag{12}$$

Equation (12) is applied up to the maximum crack width reported by Shao-feng et al.,[21] which is about $\delta_{max}=0.5$ mm. Above this threshold, $F_\delta(\delta_{max})$ is assumed. This large amplification of the reference chloride diffusion coefficient is basically intended to simulate the acceleration of the chloride penetration starting from the onset of cover spalling, which usually occurs for cracks width around 1 mm.[22] The value of δ is determined according to the experimental relationship provided by Vidal et al.[23] as a function of the loss of reinforcing steel bar cross-section area.

Several studies also pointed out the effect of concrete aging on chloride transport.[18,24] Following Muthulingam and Rao,[18] the effect of concrete age on the chloride diffusion coefficient is estimated as follows:

$$F_t = \left(\frac{t_{ref}}{t}\right)^{\mu}, \tag{13}$$

where t_{ref} [s] is the reference time of exposure, t [s] is the actual time of exposure, and μ is the age factor. It is here considered t_{ref} at 28 days and $\mu = 0.15$.

Figure 1 serves at highlighting the combined effect of different aspects on chloride transport (it is here assumed $\omega_e = 0.15$ m^3 of evaporable water/m^3 of concrete and $C_{fc} = 10$ kg/m^3 of pore solution).

2.2 | Heat transfer modeling

The heat transfer in concrete and steel is modeled in a simplified way through the Fourier's heat conduction law equation under isotropic condition, which is given by:

$$q = -\lambda\left(\frac{\partial T}{\partial x} + \frac{\partial T}{\partial y}\right), \tag{14}$$

where q [W/m^2] is the conduction heat flux, and λ [W/(mK)] is the thermal conductivity. The temperature profile is determined by applying the energy conservation law, thus obtaining:

$$\varrho c\frac{\partial T}{\partial t} = \frac{\partial}{\partial x}\left(\lambda\frac{\partial T}{\partial x}\right) + \frac{\partial}{\partial y}\left(\lambda\frac{\partial T}{\partial y}\right), \tag{15}$$

where ϱ [kg/m^3] is the density, and c [J/(kgK)] is the specific heat capacity. It is pointed out that Equation (15) is implemented under the following implicit assumptions: (i) variations of thermal conductivity, density, and specific heat capacity are small and negligible, (ii) generation of heat during hydration process is not considered, and (iii) hardened concrete does not produce or consume heat. Thermal conductivity, density, and specific heat capacity for concrete are assumed equal to 2 W/(mK), 2400 kg/m^3, and 1000 J/(kgK), respectively, whereas the corresponding values for steel are 50 W/(mK), 7850 kg/m^3, and 620 J/(kgK).

2.3 | Moisture transport modeling

It is presumed that moisture ingress takes place into concrete only. Moisture flow in concrete is commonly defined in terms of the pore relative humidity gradient as follows:

$$J_m = -D_h\left(\frac{\partial h}{\partial x} + \frac{\partial h}{\partial y}\right), \tag{16}$$

where J_m [m/s] is the moisture flux, and D_h [m/s^2] is the humidity diffusion coefficient. The corresponding mass conservation reads:

$$\frac{\partial \omega_e}{\partial h}\frac{\partial h}{\partial t} = \frac{\partial}{\partial x}\left(D_h\frac{\partial h}{\partial x}\right) + \frac{\partial}{\partial y}\left(D_h\frac{\partial h}{\partial y}\right), \tag{17}$$

where $\partial\omega_e/\partial h$ is the so-called moisture capacity. It is highlighted that Equation (17) is implemented under the following hypotheses: (i) drop in humidity due to self-desiccation is small and negligible and (ii) effect of heat in moisture transport is ignored, because the contribution of this term is rather small for the range of temperature values of interest.

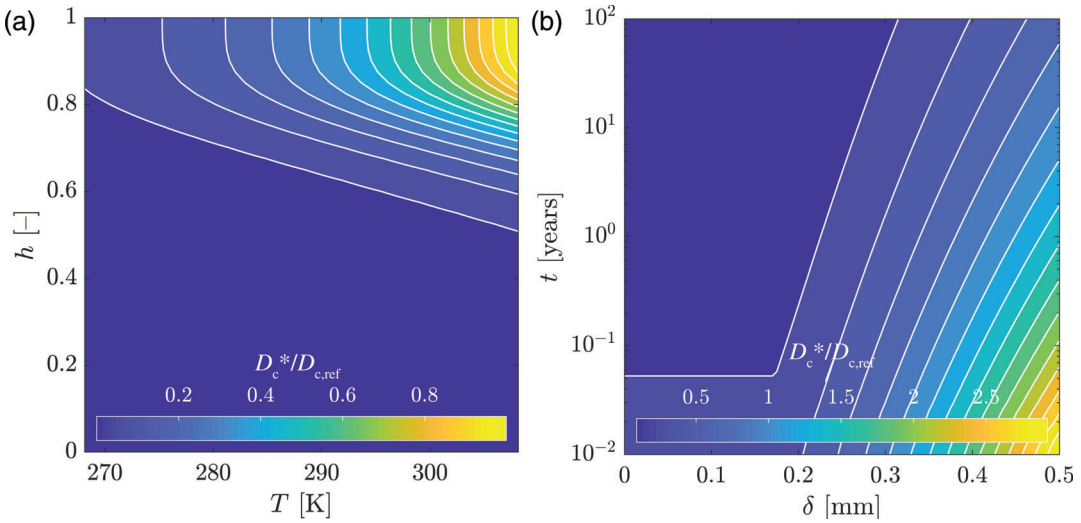

FIGURE 1 Values of $D_c^*/D_{c,ref}$ for uncracked concrete after 28 days as a function of T and h (up). Values of $D_c^*/D_{c,ref}$ for temperature and pore relative humidity equal to 296.15 K (23°C) and 0.75, respectively, as a function of δ and t (down)

2.3.1 | Adsorption isotherm

Under the hypothesis that moisture diffusion is a slow process, it can be assumed that vapor, capillary water, and adsorbed water are always in thermodynamic equilibrium. This allows to relate h and ω_e through a sorption isotherm. The most common adopted is the Brunauer–Skalny–Bodor model, which reads:

$$\omega_e = \frac{CkV_m h}{(1-kh)[1+(C-1)kh]}, \tag{18}$$

with ω_e [g of evaporable water/g of cement], where C, k, and V_m are the model parameters. The moisture capacity is, thus, obtained as follows:

$$\frac{\partial \omega_e}{\partial h} = \frac{\begin{array}{c} CkV_m + \omega_e h[1+(C-1)kh] \\ -\omega_e h(1-kh)(C-1) \end{array}}{(1-kh)[1+(C-1)kh]}, \tag{19}$$

with $\partial\omega_e/\partial h$ [g of evaporable water/g of cement]. It is noted that ω_e [m^3 of evaporable water/m^3 of concrete] and $\partial\omega_e/\partial h$ [m^3 of evaporable water/m^3 of concrete] are obtained given the cement content c [kg/m^3 of concrete]. The model parameters C, k, and V_m are defined following the assumptions by Muthulingam and Rao.[18]

2.3.2 | Humidity diffusion coefficient

Several physical, chemical, and mechanical concurrent phenomena have influence on the moisture transport. In the present study, the variability of the humidity diffusion coefficient is modeled as follows:

$$D_h = D_{h,ref} G_T(T) G_h(h) G_{t_e}(t_e), \tag{20}$$

where $D_{h,ref}$ [m^2/s] is the reference humidity diffusion coefficient (i.e., D_h value for reference conditions), and it is assumed to be the constant over all the domain. The parameters $G_T(T)$ and $G_h(h)$ are the corrective factors of the humidity diffusion coefficient that take into account the effects due to temperature T [K] and pore relative humidity h, respectively, whereas $G_{t_e}(t_e)$ accounts for those related to the hydration age. It is here assumed $D_{h,ref} = 2.00 \cdot 10^{-11}$ m^2/s.

The parameters $G_T(T)$ are defined as follows:

$$G_T = \exp\left[\frac{U_h}{R_G}\left(\frac{1}{T_{ref}} - \frac{1}{T}\right)\right], \tag{21}$$

where U_h [kJ/mol] is the activation energy of the humidity diffusion process. Herein, it is considered $U_h = 22$ kJ/mol.

On the other hand, $G_h(h)$ is evaluated by means of the following formulation[25,26]:

$$G_h = \alpha_o + \frac{1-\alpha_o}{1+\left(\frac{1-h}{1-h_c}\right)^{\eta}}, \tag{22}$$

where α_o is assumed equal to 0.05, and it is almost constant for different concrete or cement pastes. The exponent η typically varies between 6 and 16, and it is here assumed an average value equal to 10 as in some previous studies.[18]

Finally, $G_{t_e}(t_e)$ is calculated as follows[27]:

$$G_{t_e} = 0.3 + \sqrt{\frac{13}{t_e}}, \tag{23}$$

where t_e [days] is the equivalent hydration period.[26] Figure 2 serves at highlighting the combined effect of different aspects on moisture transport (it is here considered $t_e = 180$ days).

2.4 | Corrosion current density

The corrosion current density i_{corr} [μA/cm^2] is estimated by solving the governing nonlinear partial differential equations through the FE method by means of the

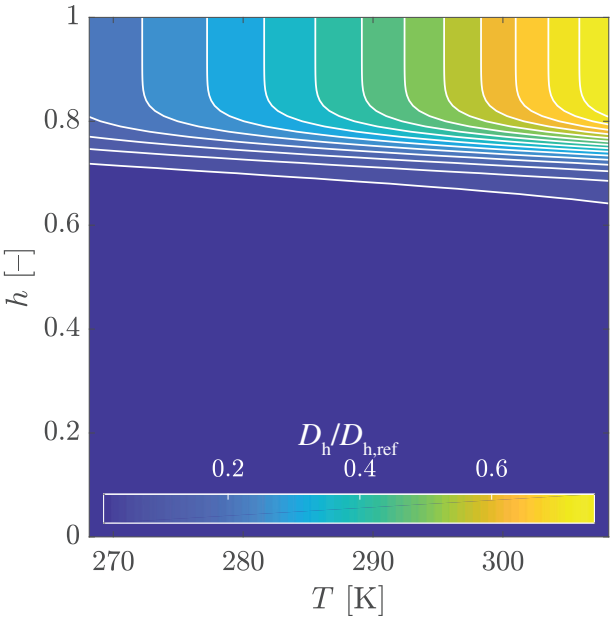

FIGURE 2 Values of $D_h/D_{h,ref}$ as a function of T and h

program COMSOL Multiphysics 5.3. Specifically, the following relationship is adopted[28]:

$$\ln 1.08 i_{corr} = 7.89 + 0.7771 \ln 1.69 C_{tc} - \frac{3006}{T} - 0.000116 R_c + 2.24 t^{-0.215}, \quad (24)$$

with t [years]. In Equation (24) R_c is the ohmic resistance of concrete, which decreases as the amount of chloride increases as proposed by Liu.[29]

3 | CORROSION PATTERN AND STRUCTURAL MODELING OF CORRODED RC BRIDGE COLUMNS

The corrosion current density as estimated from the multiphysics FE based analysis is then employed to quantify, both, geometrical and mechanical effects of chlorides-induced corrosion on rebars. Compared with previous studies on the assessment of RC bridge members under corrosion,[5–7] the present analysis accounts for the pattern of the corrosion process, proposes a novel formulation for the ultimate tensile strain of corroded rebars, and implements a refined nonlinear model for corroded reinforcing steel bars with buckling in compression. This section is intended to illustrate the way by which the effects of chlorides-induced corrosion are evaluated, together with the nonlinear FE model developed to simulate the cyclic response of RC bridge columns.

3.1 | Pitting morphology and corrosion pattern

Under chloride ingress, localized (pitting) corrosion usually takes place together with generalized corrosion[30,31]; see Figure 3. Localized corrosion occurs with the formation of large major pits whereas a cluster of minor pits along the cross-section boundary of the bar leads to a generalized corrosion.[32] Corrosion pattern (viz., number, position, and morphology of the pits as well as the relationship between localized and generalized corrosion) is expected to affect the structural response of RC members.

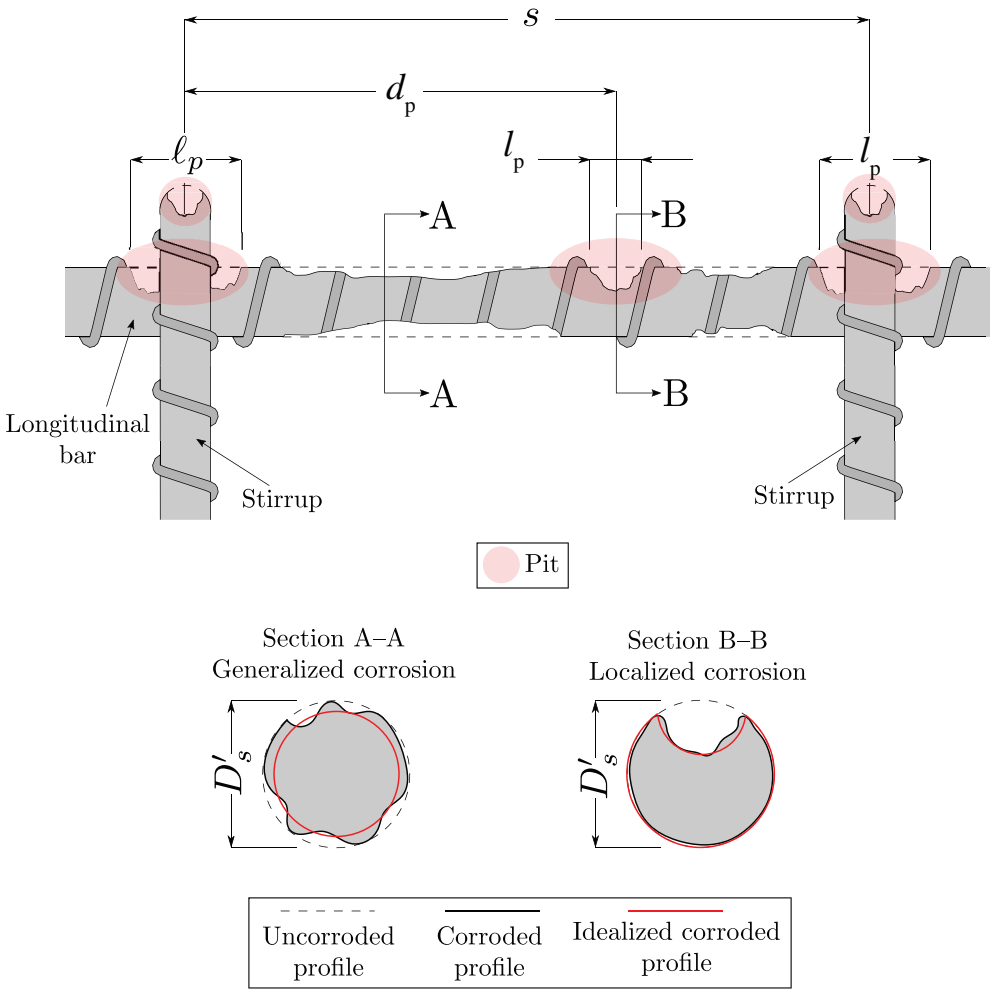

FIGURE 3 Schematic view of the corrosion pattern

As regards the localized corrosion, the increment of the pit depth Δp [mm] is evaluated as follows[33]:

$$\Delta p = 0.0116 i_{corr} \Delta t R, \tag{25}$$

where Δt [years] is the time step, and R is the pitting factor, which typically lies between 4 and 8.[33] In the present study, severe exposure conditions to chlorides will be assumed, and a mid-high severity of the pitting corrosion is considered with $6 \le R \le 8$. At each time instant, the pit depth p [mm] is obtained as cumulative sum of the corresponding previous increments Δp. The area of the corroded reinforcing steel bar A_t^p [mm^2] at the cross-section affected by localized corrosion is:

$$A_t^p = A_s' - A_p, \tag{26}$$

where A_s' [mm^2] is the original (uncorroded) area of a reinforcing steel bar whose uncorroded diameter is D_s'. The loss of reinforcing steel bar cross-section area under localized corrosion A_p [mm^2] is herein modeled, assuming a circular pit morphology according to the model developed by Val and Melchers[33]:

$$A_p = \begin{cases} A_1 + A_2 & \text{if } p \le D_s'/\sqrt{2} \\ A_{s'} - A_1 + A_2 & \text{if } D_s'/\sqrt{2} < p \le D_s' \\ A_{s'} & \text{if } p > D_s' \end{cases}, \tag{27a}$$

$$A_1 = \frac{1}{2}\left[\theta_1 \left(\frac{D_s'}{2}\right)^2 - a\left|\frac{D_s'}{2} - \frac{p^2}{D_s'}\right|\right], \tag{27b}$$

$$A_2 = \frac{1}{2}\left[\theta_2 p^2 - a\frac{p^2}{D_s'}\right], \tag{27c}$$

$$a = 2p\sqrt{1 - \left(\frac{p^2}{D_s'}\right)^2}, \tag{27d}$$

$$\theta_1 = 2\arcsin\frac{a}{D_s'}, \theta_2 = 2\arcsin\frac{a}{2p}. \tag{27e}$$

The generalized corrosion is idealized as a uniform reduction of the rebar cross-section. The area of the corroded reinforcing steel bar A_t^g [mm^2] at the cross-section affected by generalized corrosion is:

$$A_t^g = A_s' - A_g, \tag{28}$$

where A_g [mm^2] is the loss of reinforcing steel bar cross-section area under generalized corrosion. In the present study, this is parameterized as follows:

$$A_g = \rho A_p. \tag{29}$$

If the magnitude of localized and generalized corrosion is approximately the same, then $A_g \approx A_p \rightarrow \rho \approx 1$. Conversely, if generalized corrosion is negligible with respect to localized corrosion, then $A_g \approx 0 \rightarrow \rho \approx 0$.

It is presumed that where a pit takes place, it dominates the loss of the reinforcing steel bars cross-section. In other words, no generalized corrosion is considered where a pit exists whereas the vice versa holds true otherwise.

3.2 | Stress–strain relationship for bare steel bars

In what follows, the models implemented for the analysis of a bare steel bar in tension or compression are introduced, because they will serve at identifying the parameters adopted for the nonlinear modeling of the RC bridge column. The steel bar is modeled by neglecting the stress concentration due to the eccentricity originating from non-uniform rebar corrosion in the cross-section where a pit occurs. Material properties of the rebars are assumed to be unaffected by corrosion.[34]

The virgin strain–stress relationship of the bare steel bar under tension is assumed to be elastic with linear hardening. Furthermore, constant strain fields with different strain magnitudes are considered; see Figure 4. Two corrosion indices are also defined, namely $\mu_{pit} = 1 - A_t^p/A_s'$ and $\mu_{rel} = 1 - A_t^p/A_t^g$.

The failure condition of the corroded rebar corresponds to the attainment of the ultimate strain ε_{su}' in the pit, which implies an average ultimate strain ε_{su} over the reference length L given by:

$$\varepsilon_{su} = \frac{\varepsilon_{su}' \ell_p + \varepsilon_s^g (L - \ell_p)}{L}, \tag{30}$$

where ε_{su}' is the ultimate strain of the uncorroded steel, and ε_s^g is the strain level in the reinforcing steel bar under generalized corrosion. The reference length L is assumed equal to the distance s between two transverse reinforcement positions. The parameter ε_s^g is estimated as follows:

$$\varepsilon_s^g = \begin{cases} \dfrac{f_{su}^*(1-\mu_{rel})}{E_s} & \text{if } \mu_{rel} \ge \mu_{cr} \\ \dfrac{f_{sy}'(b-1) + f_{su}^*(1-\mu_{rel})}{bE_s} & \text{if } \mu_{rel} < \mu_{cr} \end{cases}, \tag{31}$$

where f_{sy}' is the yield stress of the uncorroded reinforcing steel bar, and E_s and b are Young's modulus and hardening ratio of the uncorroded reinforcing steel bar,

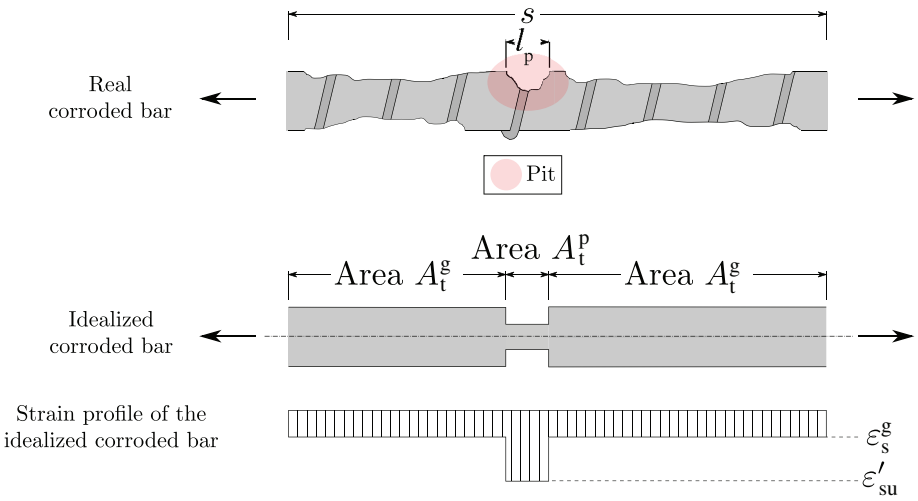

FIGURE 4 Idealization of the corroded longitudinal reinforcing bare steel bar under tension and identification of the strain profile

respectively. Moreover, f^*_{su} is the actual ultimate stress of the uncorroded reinforcing steel bar based on the instantaneous cross-section area,[35] with $f^*_{su} = f'_{su}(1+\varepsilon'_{su})$, where f'_{su} is the engineering ultimate stress based on the nominal cross-section area of the uncorroded reinforcing steel bar. Finally, the parameter $\mu_{cr} = 1 - f'_{sy}/f^*_{su}$ is the critical corrosion level[36]; i.e., the corrosion level above which the bar outside the pit would not yield upon the failure in the pit. The proposed model is validated against available experimental data[37]; see Figure 5. In general, it can be observed that the proposed model is in good agreement with the experimental data until $\mu_{pit} = 20\%$. Otherwise, it underestimates the ultimate strain of the corroded bar. This might be due to the fact that available experimental data refer to Tempcore bars, which have a heterogeneous cross-section with a martensitic crown (outside layer) stronger and less ductile than the ferrite core (inner layer).[38] For sake of completeness, it also illustrated the proposed model for a Tempcore bar in which $\varepsilon'_{su} = 20\%$ is adopted for $\mu_{pit} > 30\%$ (this value is here adopted because the area of the martensitic crown for the tested bar having a 12 mm nominal diameter was found to be about 30% of the total cross-section area[39]).

Regarding the analysis of the bare steel bar in compression, a force-based beam-column element is considered under large displacements via corotational transformation.[40,41] The virgin strain–stress relationship of the bare steel bar under compression is assumed according to the Giuffré–Menegotto–Pinto model[42] with isotropic strain hardening.

The adopted buckling length L_b to evaluate the bare steel bar response in compression is equal to the distance between transverse reinforcement s (local buckling) or to an integer multiple of it (global buckling).[43] The occurrence of local or global buckling depends on the stiffness of transverse reinforcement (which provides the lateral constraint to the longitudinal rebars) and the inertia of longitudinal rebars. As corrosion reduces the area of transverse

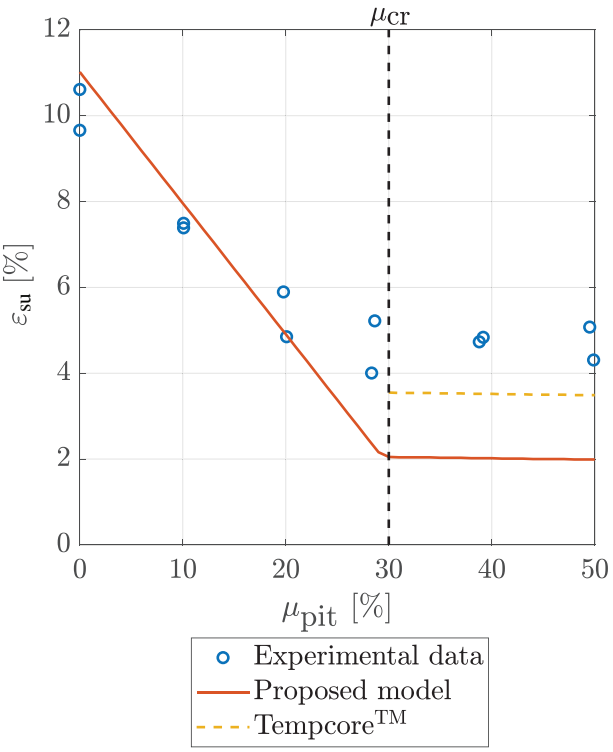

FIGURE 5 Relationship between μ_{pit} and ε_{su} under tension

reinforcement and its lateral constraint capability, the buckling length of longitudinal reinforcement can increase during time. On the other hand, corrosion also reduces the inertia of the longitudinal rebars, which thus require a lower level of lateral constraint to prevent buckling.

3.3 | Numerical FE model

The nonlinear FE model of the RC bridge column has been developed into the OpenSees platform. The cross-sections of the column are discretized into several

unidirectional steel and concrete fibers. The resulting discretized model employs force-based fiber elements,[44,45] and the Gauss–Lobatto integration scheme is adopted when appropriate. It is known that force-based elements can lack of objectivity at local or global level, depending on the hardening/softening-type response.[46] In this sense, the post-buckling softening-type response of reinforcing steel bars under compression has significant impact on strain localization at the critical sections. Hence, it has been recommended to assume the integration length of the base first integration point (where buckling is expected to occur) equal to L_b.[9] As the Gauss–Lobatto integration scheme does not allow adjusting the length of the first integration point, this requires the use of two force-based elements. The first one (lower element) has a length equal to $6L_b$ and three Gauss–Lobatto integration points. This makes the length of the first integration point equal to L_b. Conversely, a force-based element with five integration points is employed for the second element (upper element).[47] When L_b is larger than the distance between two transversal reinforcements, the Newton–Cotes integration scheme with two integration points is adopted for the first element. The length of the first element, in this case, is considered to be twice the buckling length of the longitudinal reinforcement.

Moreover, a rigid link is introduced to connect the column tip in the FE model (i.e., intersection between column vertical axis and pier cap longitudinal axis) with the point where axial and lateral force are applied (i.e., bridge bearing). A zero-length section at the base of the column is used to simulate the strain penetration of the anchorage reinforcement in the footing. Herein, a displacement–stress relationship is assigned at each fiber instead of the strain–stress one. In detail, the slip–stress constitutive model developed by Zhao and Sritharan[48] is assigned to the reinforcing steel bars. This is accomplished into OpenSees by means of the uniaxial material model `Bond_SP01`. In doing so, the anchorage reinforcement in the footing is presumed to be protected against aggressive chemicals, and thus, the footing reinforcement is assumed to be not affected by corrosion. The displacement–stress relationship for concrete is obtained by multiplying the strains of the Kent–Scott–Park strain–stress model[49,50] by an effective depth $d_{comp} = 0.3D$ over which the compression strain takes place[9,47] (where D is the diameter of the RC bridge column).

The overall FE model of the RC bridge column is shown in Figure 6.

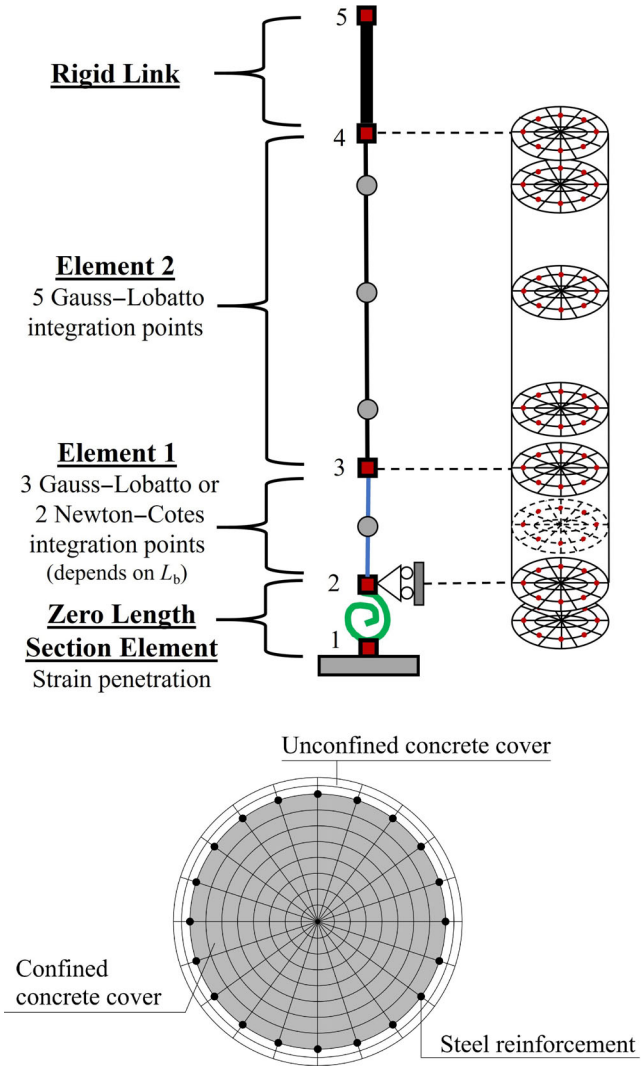

FIGURE 6 Structural FE model of the RC bridge column (up) and detail of the cross-section discretization (down)

3.3.1 | Strain–stress relationship for concrete

The uniaxial material model Concrete01 available into OpenSees is employed to simulate the behavior of the unconfined cover concrete. It implements the Kent–Scott–Park strain–stress model,[49,50] where a parabolic curve in the pre-peak stage and a linear softening curve in the post-peak response are assumed under compression whereas a null tensile strength is considered under tension. For the unconfined concrete, the falling branch reaches zero stress for the spalling strain value equal to 0.4% in uncorroded condition. The effects of concrete cover cracking and spalling due to rust production are also taken into account. Specifically, the strength of the cover concrete is reduced by adopting a brittle post-peak behavior as suggested by Coronelli and Gambarova.[51] The reduced concrete cover strength f_c is evaluated as follows:

$$f_c = \frac{f'_c}{1 + K\bar{\varepsilon}_1/\varepsilon'_c}, \tag{32}$$

where f'_c is the nominal compressive strength of sound concrete, K is a coefficient related to bar roughness and

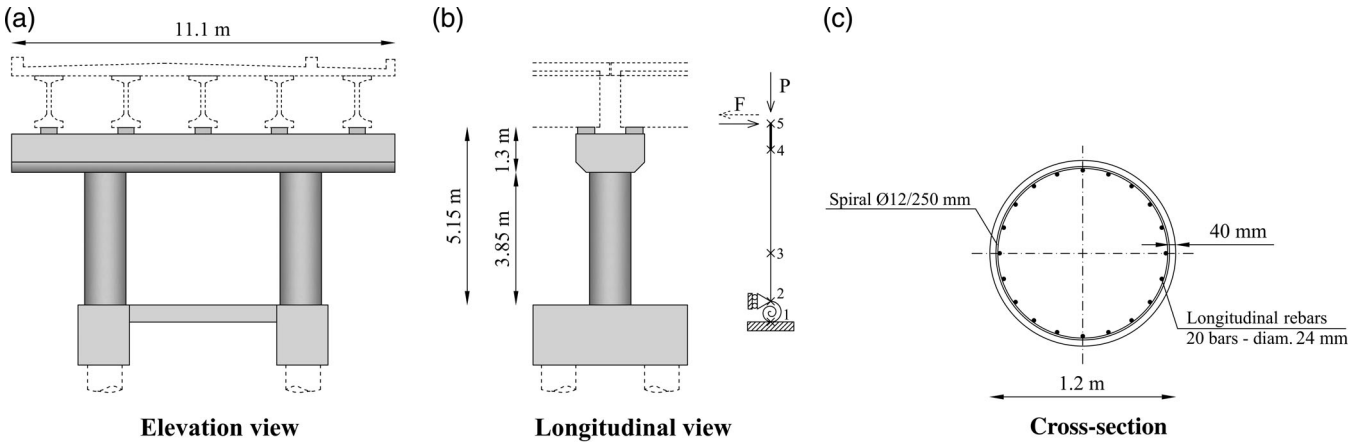

FIGURE 7 Layout of the case study

TABLE 1 Corrosion scenarios for the longitudinal rebars in-between the transverse reinforcement (they apply to all D'_s values)

Scenario label	Additional pitting corrosion: Additional pit(s)/pitting factor/pit(s) position	Additional pitting corrosion: Pit(s) length	Generalized corrosion
0p	None	–	$\rho = 0$
1p6-50-0	One pit/$R = 6/d_p = 0.50s$	$\ell_p = 0.50D'_s$	$\rho = 0$
1p6-150-0	One pit/$R = 6/d_p = 0.50s$	$\ell_p = 1.50D'_s$	$\rho = 0$
1p6-150-50	One pit/$R = 6/d_p = 0.50s$	$\ell_p = 1.50D'_s$	$\rho = 0.50$
2p6-150-0	Two pits/$R = 6/d_p = 0.33s$ and $d_p = 0.66s$	$\ell_p = 1.50D'_s$	$\rho = 0$
2p6-150-50	Two pits/$R = 6/d_p = 0.33s$ and $d_p = 0.66s$	$\ell_p = 1.50D'_s$	$\rho = 0.50$
1p8-100-0	One pit/$R = 8/d_p = 0.50s$	$\ell_p = 1.00D'_s$	$\rho = 0$

Note: One pit ($R = 8$) with $\ell_p = 1.00D'_s$ is always assumed in the longitudinal rebar at the level of the transverse reinforcement.

diameter ($K = 0.1$ can be adopted for ribbed bars), and ε'_c is the strain value corresponding to f'_c. Moreover, $\overline{\varepsilon}_1$ is the average tensile strain of the cracked concrete.[52]

On the other hand, the uniaxial material model Concrete04 available into OpenSees is employed to simulate the behavior of confined core concrete. This model implements the strain–stress relationship proposed by Popovics[53] for loading in compression. It is also implemented into the concrete model proposed by Mander et al.,[54] which is adopted to account for the confinement due to the transverse reinforcement. The effect of transverse reinforcement corrosion on core concrete confinement is modeled in a simplified, yet conservative, way by referring to the time-varying value of its corroded cross-section area.

3.3.2 | Strain–stress relationship for reinforcing steel bars

The strain–stress relationship adopted in the present work for the longitudinal reinforcement is a modified Monti–Nuti uniaxial material model[55–57] SteelMN developed ad hoc into OpenSees (note that it is an in-house material model for OpenSees not publicly available yet). Its complete formulation is also reported in *fib* Bulletin 2020.[58] The model represents a generalized cyclic stress–strain characterized by isotropic and kinematic hardening with possible inelastic buckling in compression. Menegotto–Pinto-type skeleton curves[42] are herein implemented, which are constituted by straight segments. Elastic and plastic branches are characterized by elastic modulus, hardening ratio, yielding, and inversion point coordinates in the strain–stress plane. The bare steel bars model presented previously has been employed, considering the relevant corrosion morphologies to estimate all the involved parameters. For sake of completeness, it is recalled that this model for corroded rebars is very accurate if the strain in compression is smaller than 1.5%; otherwise, its accuracy slightly reduces. This is compatible with failure conditions in the following numerical investigation. In general, previous investigations have demonstrated that larger deformation values seldom occur in realistic RC members[59] at the compressed reinforcement level.

3.3.3 | Buckling length of the longitudinal reinforcement

The buckling length L_b depends on both flexural rigidity of longitudinal rebars and stiffness of the transverse reinforcement. Therefore, buckling length can change the buckling mode from being local to global during the service life of the bridge column because of the corrosion. The iterative procedure proposed by Dhakal and Maekawa[60] is here considered to evaluate the effective buckling length. It is an energy-based methodology that allows to calculate the stiffness required to sustain the nth buckling mode (where n is the number of spiral pitches involved in the buckling mode). The required stiffness is thus compared with the current stiffness of the transverse reinforcement to establish the actual buckling mode (i.e., to find the value of n). The iterative procedure ends when the required stiffness to support the nth buckling mode is less than the current stiffness. This methodology was later implemented by Kashani et al.[61] for corroded rebars under the following simplified assumptions: (i) the current minimum inertia value of the corroded longitudinal reinforcement I_{min} is adopted for evaluating the flexural rigidity of longitudinal reinforcement instead of the value referred to the uncorroded bars and (ii) the uncorroded area of the transverse reinforcement A'_s is replaced with the current minimum corroded value A_s for evaluating its stiffness. Hence, the current flexural rigidity of the longitudinal corroded bars EI_t is calculated as follows[60]:

$$EI_t = \frac{E_s I_{min}}{2}\sqrt{\frac{f'_{sy}}{400}}. \tag{33}$$

The (time-dependent) stiffness of the corroded spiral confinement K_t is evaluated according to the empirical formulation proposed by Pantazopolou[62]:

$$K_t = \frac{4E_s A_s}{\sqrt{s^2 + d_c^2}}, \tag{34}$$

where d_c is the core diameter.

4 | NUMERICAL INVESTIGATION

4.1 | Case study

The reference layout of the case study herein considered for the following parametric investigations is derived from a real RC bridge located in Sardinia (Italy), which is illustrated in Figure 7. The deck is made of simple multi-span precast concrete girders supported by rigid frame column. The selected bridge column has a height equal to 3.85 m (up to the pier cap) and a circular cross-section with diameter equal to 1.2 m. The original longitudinal reinforcement consists of 20 rebars with diameter equal to 24 mm placed on a single concentric circular layer. Longitudinal rebars with diameter equal to 20 and 28 mm are also considered to investigate the influence of different diameters (the geometrical reinforcement ratio is kept constant). Moreover, there is a spiral confinement whose diameter and spacing are equal to 12 and 250 mm, respectively. The concrete

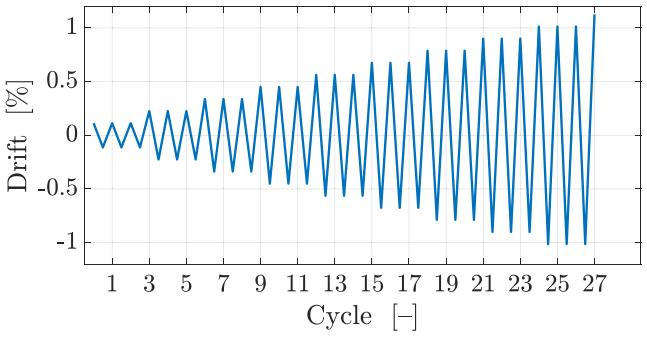

FIGURE 8 Imposed drifts for the nonlinear cyclic analyses of the RC bridge column

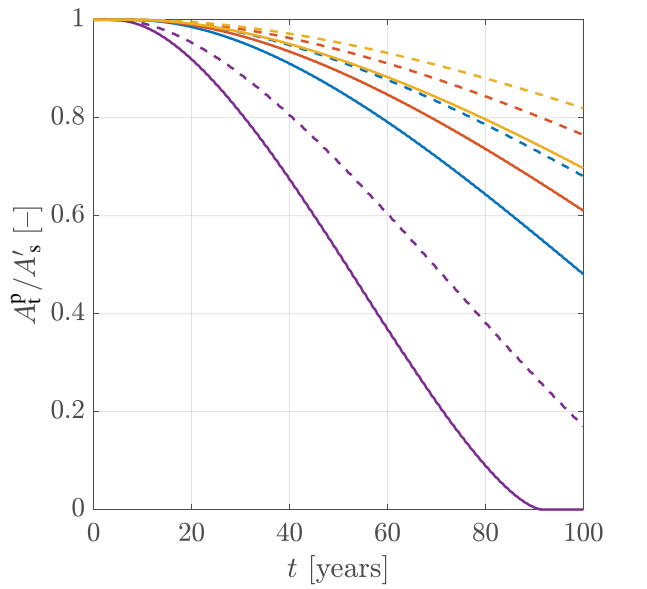

FIGURE 9 Ratio A_t^p/A'_s for different values of R and D'_s

cover depth is equal to 40 mm, and the axial load on the single column is estimated equal to $P = 4500$ kN. As the main goal of the present study is to investigate the cyclic behavior of corroded RC bridge columns, a single pier is analyzed in the longitudinal direction, which can be effectively modeled as a cantilever element (by neglecting the effect due to the frame).

Mechanical proprieties of sound concrete are assumed to be $f'_c = 30.0$ MPa and $\varepsilon'_c = 0.2\%$. Average uncorroded mechanical proprieties of the reinforcing steel bars are assumed as $f'_{sy} = 536.00$ MPa, $f'_{su} = 649.00$ MPa, and $\varepsilon'_{su} = 11.6\%$ following Apostolopoulos et al.[63]

4.2 | Solution methods and data

The time evolution of the pitting corrosion in the RC bridge column cross-section was assessed by means of multiphysics simulations throughout a lifespan equal to 100 years. A null initial chloride concentration is considered within the cross-section whereas the initial values of temperature and pore relative humidity are taken as 296.15 K and 0.65, respectively. A total surface chloride content of 7 kg/m^3 of concrete is assumed, which is representative of exposure conditions close to the Mediterranean coasts. Temperature and relative humidity on the boundary vary according to $T = 296.15 - 15\sin(2\pi t/365)$ [K] and $h = 0.65 + 0.15\sin(\pi t/365)$, respectively, with t [days]. The analyses were performed for pitting factor values equal to 6 and 8.

The parametric study is detailed in Table 1. Corrosion scenarios differ in terms of pitting corrosion pattern for the longitudinal rebars in-between the transverse reinforcement. For all corrosion scenarios, it is assumed that a localized corrosion also occurs in the longitudinal reinforcing steel bar at the level of the transverse reinforcement, in agreement with several laboratory evidences and field surveys.[30,31,64] Corrosion scenario cases are labeled as follows: number of pits on the longitudinal rebars in-between the transverse reinforcement/p/pitting factor—ratio between pit length and longitudinal rebar diameter in percent—ratio between loss of reinforcing steel bar cross-section area under generalized corrosion and that due to pitting corrosion in percent. It is pointed out that pit length values ℓ_p in Table 1 are assumed as given numerical data for the parametric study, and they are consistent with reported experimental evidences.[31,65]

The parametric analyses campaign has been planned as follows. The comparison among the cases 0p, 1p6-50-0, 1p6-150-0, and 1p8-100-0 is meant at investigating what is the difference if none or one pit in-between the transverse reinforcement spacing is assumed, taking also into account the influence of pitting factor and pit length. On the other hand, the comparison between case 1p6-150-0

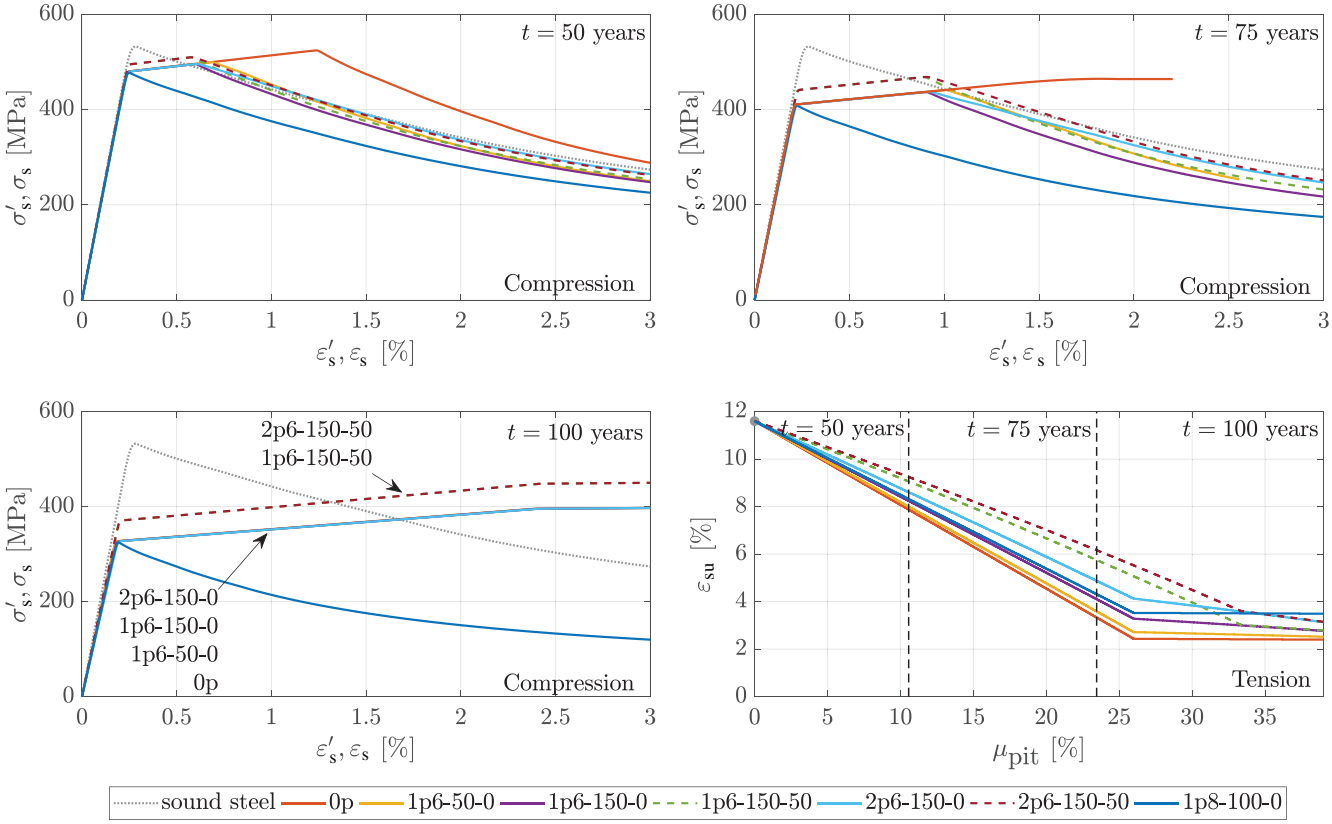

FIGURE 10 Strain–stress relationships for bare steel bar with $D'_s = 24$ mm for constant local buckling mode (i.e., $L_b = s$)

and case 1p6-150-50 serves at understanding the influence of a simultaneous generalized corrosion. Two pits in-between the transverse reinforcement spacing are considered in cases 2p6-150-0 and 2p6-150-50, taking also into account the influence of the generalized corrosion besides the localized one in the latter. Nonlinear cyclic analyses are performed under displacement-controlled conditions. The imposed drifts are reported in Figure 8.

It is understood that the following numerical study is meant at understanding the time-dependent flexural behavior of the column while the shear capacity is not discussed. However, for the present case study, it has been estimated according to the model proposed by Kowalsky and Priestley[66] that the shear capacity (without considering the contribution due to the transverse reinforcement) is always higher than the shear demand.

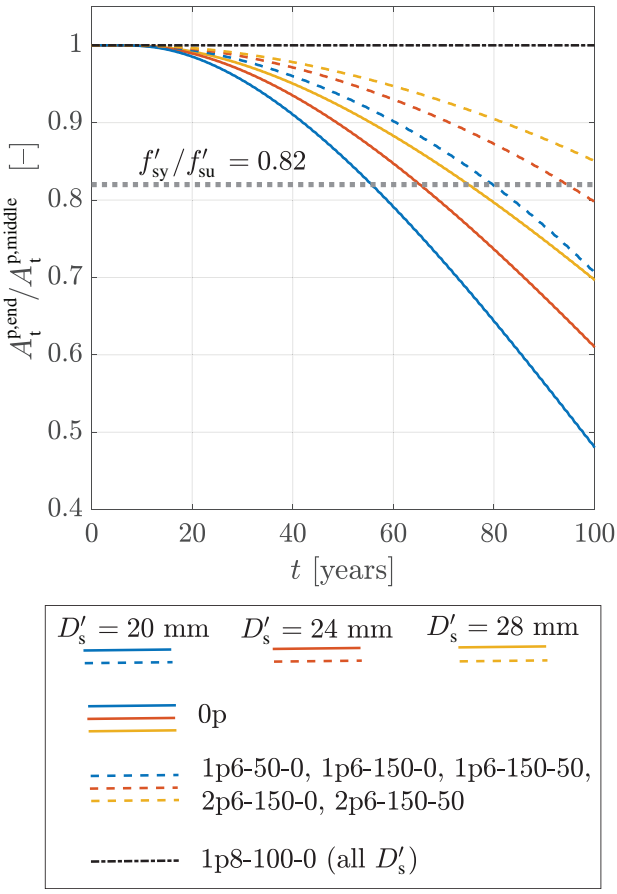

FIGURE 11 Ratio $A_t^{p,end}/A_t^{p,middle}$ for different values of D'_s at varying corrosion scenarios

4.3 | Parametric study

The time-dependent evolution of the pitting corrosion predicted from multi-physics FE based simulations is illustrated in Figure 9. As expected, the lower the diameter of the reinforcing steel bars, the larger the effects of the pitting corrosion. For the considered set of longitudinal rebar diameters, the corroded area as consequence of the pitting corrosion ranges from 5% to 10% at $t = 50$ years, whereas it varies between 20% and 30% at

TABLE 2 Values of λ at $t = 100$ years for different values of D'_s

	Data at $t = 100$ years		
D'_s [mm]	$D_{s,eq}$ [mm]	L_b [mm]	λ [–]
20	15.0	500	33.30
24	18.5	750	40.50
28	23.5	1000	42.55

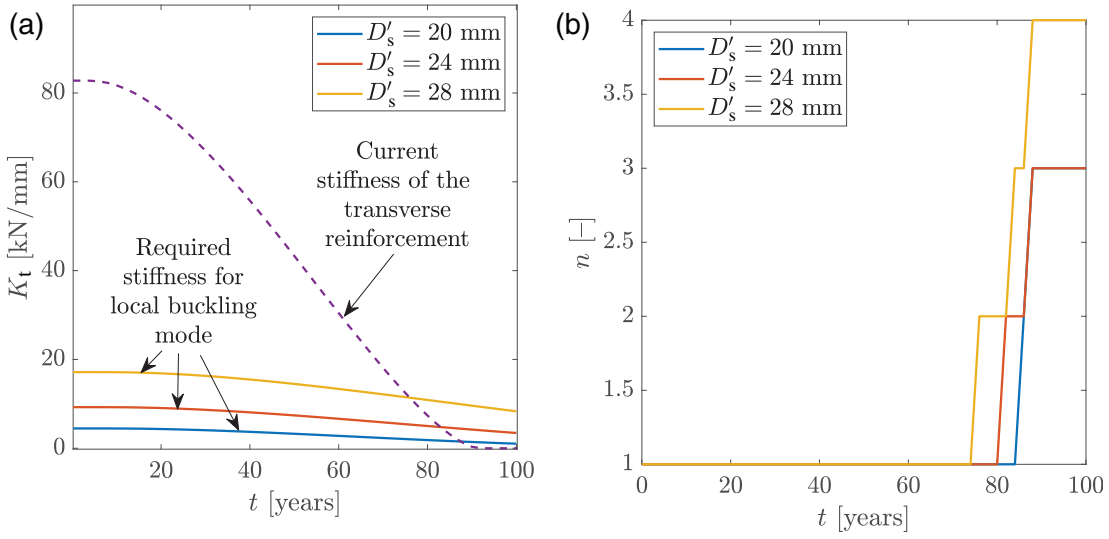

FIGURE 12 Evolution of L_b (up) and n (down) for different values of D'_s

$t = 100$ years considering $R = 6$. The larger the pitting factor, the larger the corroded area. If $R = 8$ is considered, then the corroded area in the longitudinal rebars ranges from 10% to 15% at $t = 50$ years, whereas it varies between 30% and 50% at $t = 100$ years. For $R = 8$, it is estimated that the cross-section area of the transverse reinforcement at the pit is completely corroded after about $t = 90$ years.

Figure 10 illustrates the strain–stress relationships of a bare bar with $D'_s = 24$ mm under compression at $t = \{50, 75, 100\}$ years (they are evaluated with respect to the cross-section area in the generalized corrosion region) as well as the ultimate strain in tension calculated according to Equation (30). A constant buckling length $L_b = s$ (i.e., a local buckling mode) is considered to derive the strain–stress relationships in Figure 10 for better understanding the effects of the corrosion pattern.

Figure 10 shows that a degrading branch due to the rebar buckling at $t = 100$ years occurs for the corrosion scenario 1p8-100-0 only. On the other hand, with the exception of the corrosion scenario 0p at $t = 75$ years, rebar instability at $t = \{50, 75\}$ years takes place after yielding. This can be explained by recalling that lateral instability is triggered when three aligned plastic hinges arise along the longitudinal rebar under compression. Therefore, while two plastic hinges are expected at the level of the transverse reinforcement because of the high pitting corrosion severity at these points, an additional hinge may or may not arise in-between depending on rebar yielding at the intermediate pit before failure in compression. Rebar buckling would happen until the ratio between cross-section area of the longitudinal steel bar affected by pitting corrosion at the level of the transverse reinforcement $A_t^{p,end}$, and that in the middle pit, $A_t^{p,middle}$ is greater than f'_{sy}/f'_{su}. Figure 11 shows $A_t^{p,end}/A_t^{p,middle}$ for all corrosion scenarios and rebar diameters, and it is useful to further explain the results in Figure 10. In fact, Figure 10 highlights that, since three identical pits take place in the longitudinal steel bars for the corrosion scenario 1p8-100-0, the ratio $A_t^{p,end}/A_t^{p,middle}$ turns to be equal to 1 and rebar buckling always happens in such case. For other corrosion scenarios, rebar buckling may or may not arise depending on the point in time. It can be also inferred from Figure 10 that the response under compression is slightly affected by pit length and number of pits in the middle (when larger than one). This is because the post-yield buckling response is ruled by the equilibrium of the buckled bar within two consecutive stirrups, which, in turn, depends on the plastic moments in three plastic hinges.[67]

Results in Figure 10 refer to a local mode of buckling only. However, it has been found that a global buckling mode can take place near the end of the considered lifespan. Specifically, Figure 12 illustrates that the current stiffness of the transverse reinforcement is lower than the required stiffness needed to sustain local buckling after about $t = \{86, 84, 76\}$ years for longitudinal rebar diameters equal to $D'_s = \{20, 24, 28\}$ mm, respectively. The maximum mode of buckling is achieved at $t = 90$ years and is equal to $n = \{2, 3, 4\}$ for longitudinal rebar diameters equal to $D'_s = \{20, 24, 28\}$ mm, respectively. It is pointed out that this value of n is also assumed for $t > 90$ years, because the iterative procedure for finding the buckling mode does not converge beyond such limit.

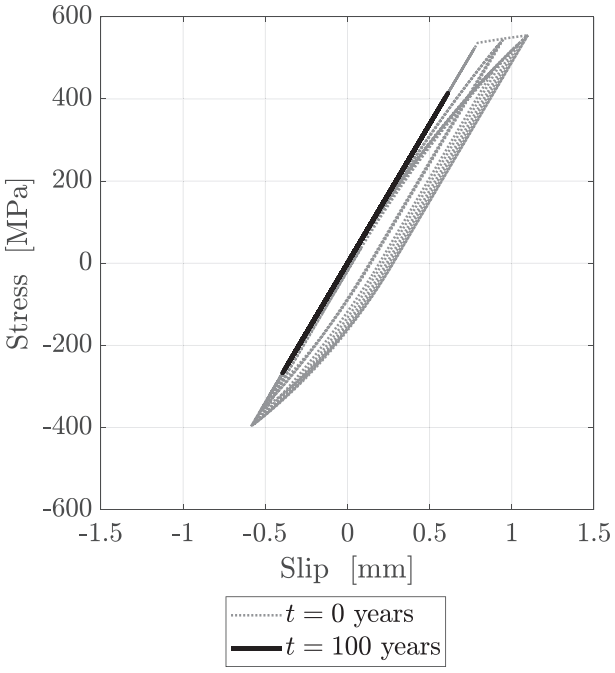

FIGURE 13 Slip–stress curve of the steel reinforcement for the zero-length section element representing the strain penetration effects

Figure 12 basically highlights the need of reconsidering the results into Figure 10 corresponding to $t = 100$ years because of the global buckling modes of the longitudinal reinforcement. Buckling will always occur in this case, because three aligned plastic hinges arise along the longitudinal rebar, and the buckling response results are affected only by the plastic moments in its most corroded sections (i.e., corrosion scenarios considered in Table 1 do not affect anymore the buckling response of the bare bar at $t = 100$ years). Table 2 provides details about the slenderness of the corroded longitudinal rebars at $t = 100$ years (herein, $D_{s,eq}$ is the equivalent corroded longitudinal rebar diameter, $L_b = n \cdot s$ and $\lambda = L_b/D_{s,eq}$).

Results in Table 2 confirmed that the slenderness ratio λ at $t = 100$ years is always greater than the critical slenderness ratio λ_{cr}. The buckling of the longitudinal

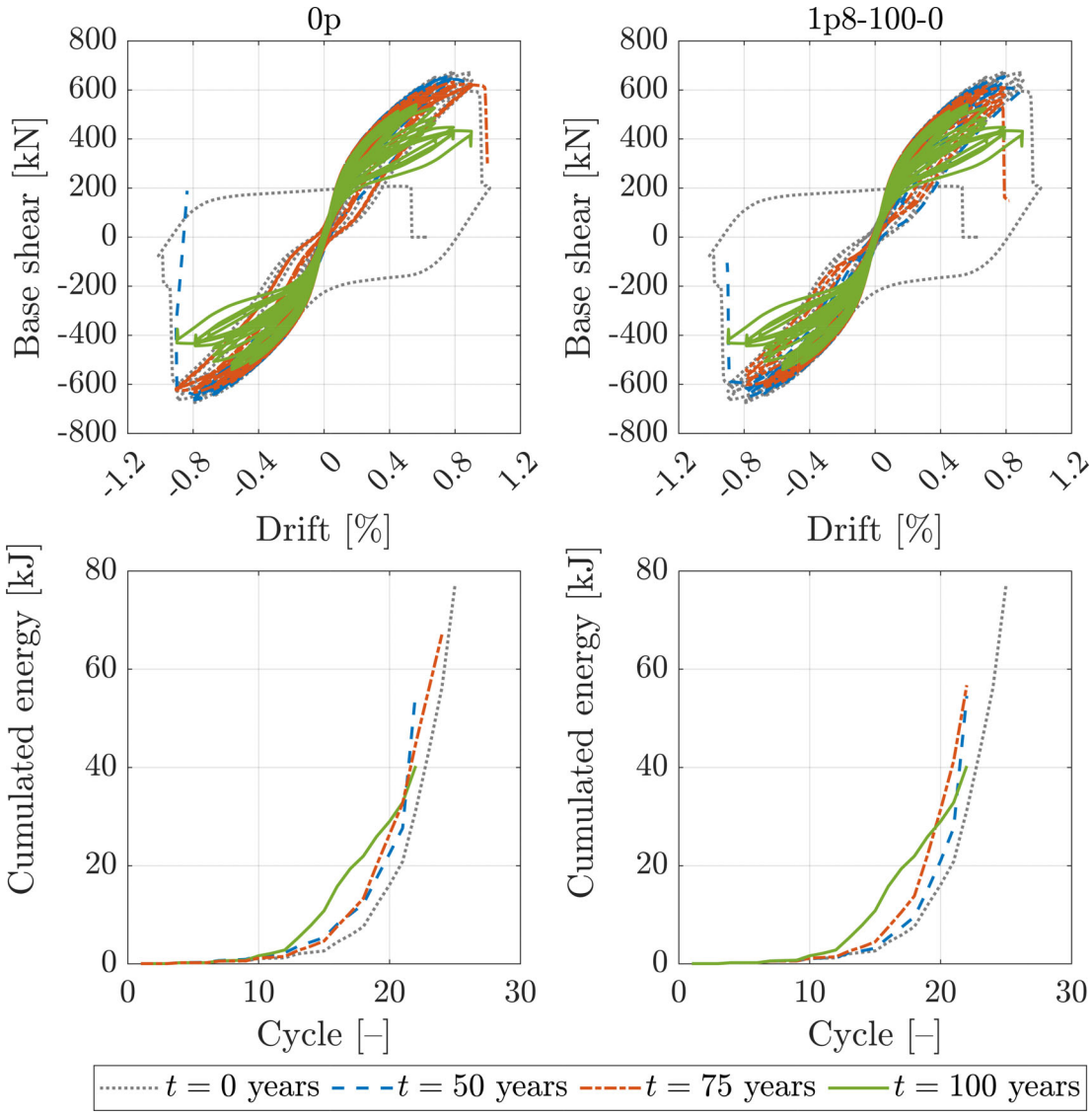

FIGURE 14 Drift versus base shear (up) and cumulated energy (down) for corrosion scenarios 0p and 1p8-100-0 at $t = \{50, 75, 100\}$ years considering $D'_s = 24$ mm

rebars is governed by Eulerian law, and the compressive post-peak behavior is almost brittle (i.e., high negative slope of the softening branch).

Figure 13 illustrates the slip–stress curve of the steel reinforcement for the zero-length section element representing the strain penetration effects at the beginning and the end of the considered time window. Some representative cycle responses in terms of drift and base shear are shown from Figures 14–16 for different corrosion scenarios, longitudinal bar diameters, and time of exposure. A comprehensive overview about the time variation of the RC bridge column response is provided in Figure 17 in terms of yielding displacement, ultimate displacement, and ductility (normalized with respect to the corresponding values for the uncorroded column). For the sake of completeness, capacity and displacement ductility of the sound column are also provided in Table 3.

Two limit scenarios are considered in Figure 14, where the case of two pits in the longitudinal rebar at the level of the transverse reinforcement (scenario 0p) is compared with a pattern consisting of an additional identical pit in the middle of the spiral pitch (scenario 1p8-100-0). These results demonstrate that the column capacity is slightly affected by the occurrence of such further localized corrosion in-between the transverse reinforcement. Conversely, the corrosion scenario has significant influence on the mid-term response (i.e., at $t = 75$ years) in terms of ductility, because local rebar buckling does not arise for the scenario 0p after about 65 years for $D'_s = 24$ mm (see Figure 11) while it always occurs for the scenario 1p8-100-0. On the other hand, the long-term responses (i.e., at $t = 100$ years) do

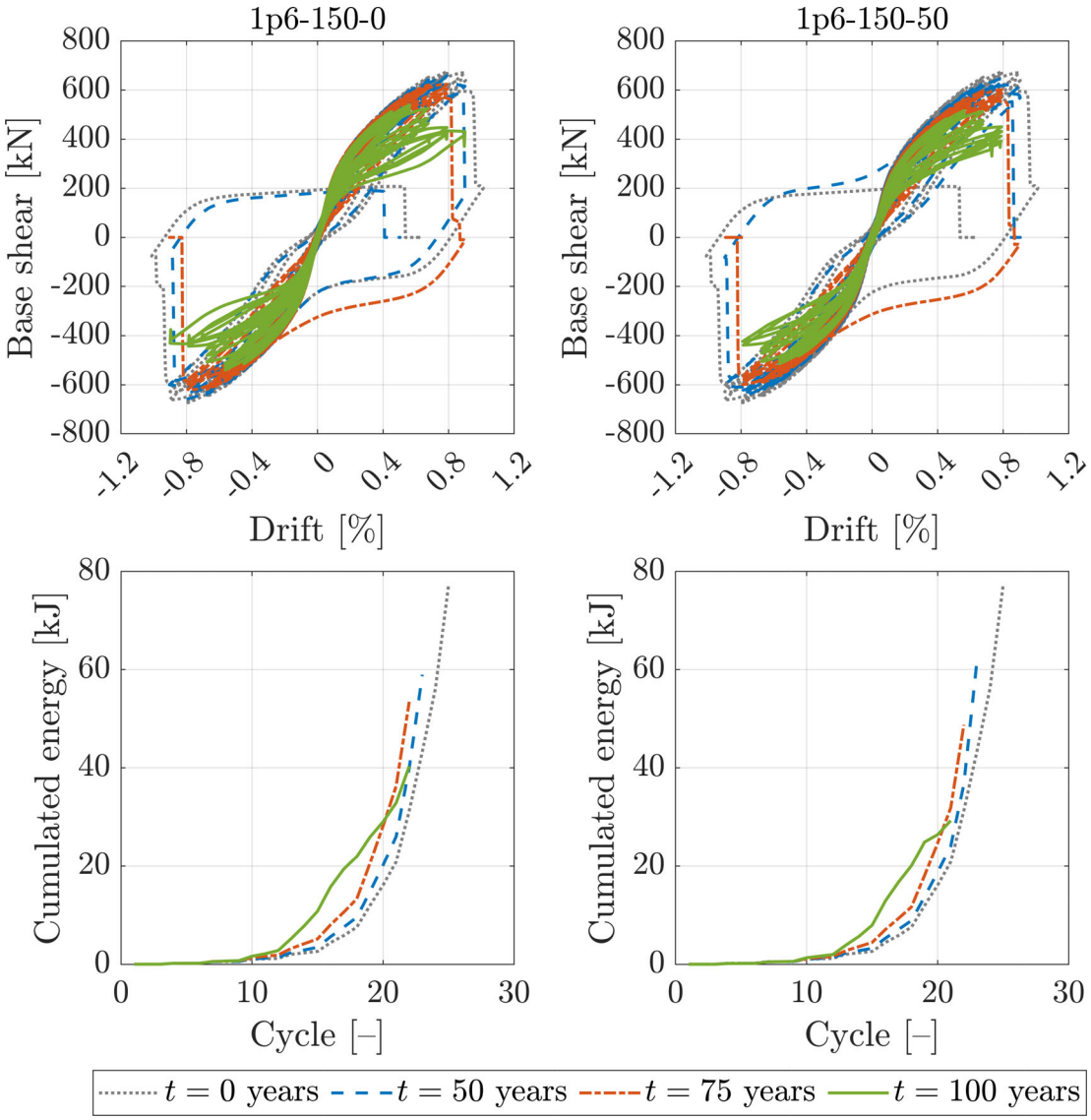

FIGURE 15 Drift versus base shear (up) and cumulated energy (down) for corrosion scenarios 1p6-150-0 and 1p6-150-50 at $t = \{50, 75, 100\}$ years considering $D'_s = 24$ mm

not depend on the corrosion scenario, because they are governed by the global rebar buckling, which arises for both scenarios after $t = 84$ years (see Figure 12). This reflects, in the different ways, the energy dissipated over time. In fact, the amount of dissipated energy reduces passing from $t = 0$ years (uncorroded case) to $t = 100$ years for the scenario 1p8-100-0 because of the loss of the reinforcing steel bar cross-section area. On the other hand, an increment of the dissipated energy is observed at $t = 75$ years for the scenario 0p even though the loss of the reinforcing steel bar cross-section area is higher than that at $t = 50$ years, because the rebar instability is prevented for such corrosion pattern after about 65 years. The amount of dissipated energy drastically decreases again in such scenario at $t = 100$ years due to the occurrence of global rebar buckling.

Figure 15 highlights the role of a generalized corrosion of the longitudinal reinforcing steel bars together with a pit in-between the transverse reinforcement. To this end, the scenarios consisting of three pits in the longitudinal rebar (i.e., two identical pits at the level of the transverse reinforcement together with a less severe pit in-between) without or with generalized corrosion are considered (namely, scenarios 1p6-150-0 and 1p6-150-50). Despite the rather large magnitude of the generalized corrosion, it seems that its effects on the column capacity are moderate, and they appear even smaller in terms of ductility. Also, the time-evolution and the amounts of dissipated energy with or without a simultaneous generalized corrosion are rather similar. This suggests that the localized corrosion is likely the most important aspect in the cyclic behavior of the considered RC bridge column.

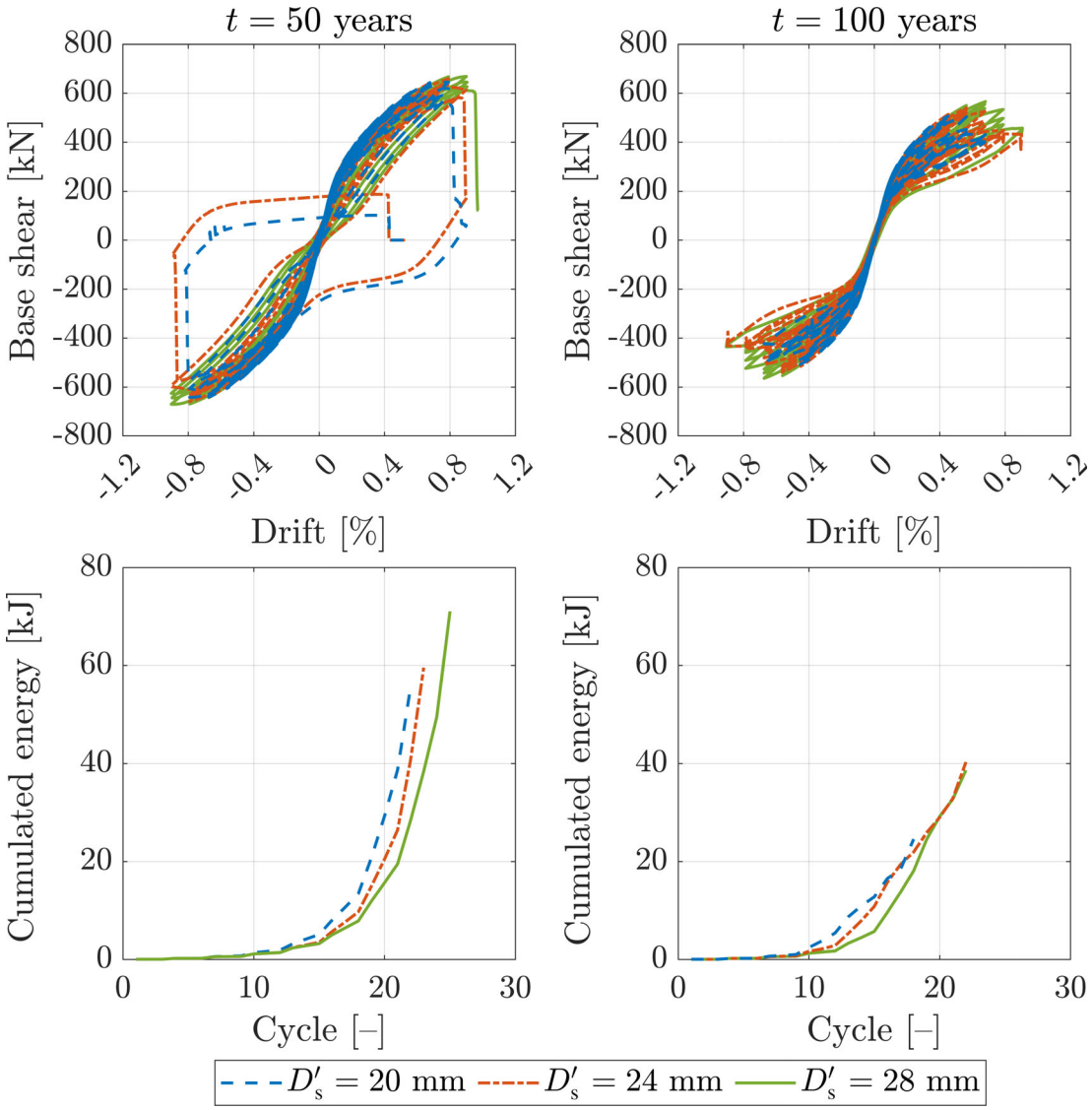

FIGURE 16 Drift versus base shear (up) and cumulated energy (down) for corrosion scenario 1p6-50-0 at $t = 50$ years and $t = 100$ years considering $D'_s = \{20, 24, 28\}$ mm

Figure 16 investigates the role of the longitudinal rebar diameter in RC bridge columns. Herein, it considered the corrosion scenario consisting of one shorter and less severe pit in the middle of the spiral pitch besides two severe pits at the level of the transverse reinforcement (scenario 1p6-50-0). As the loss of cross-section area for rebars with large diameter values is less than that for low diameter values, the reduction of the RC bridge column capacity grows up as the nominal rebar diameter reduces. The amount of dissipated energy reduces at $t = 50$ years passing from $D'_s = 28$ mm to $D'_s = 20$ mm due to the larger loss of the corroded cross-section area of the rebars. After $t = 100$ years, the dissipated energy for $D'_s = 20$ mm is especially low as compared with that for $D'_s = 24$ mm and $D'_s = 28$ mm due to premature failure.

Figure 17 show that the time variation of the yielding displacement with respect to the capacity is almost linear. While a monotonic trend is observed in terms of yielding displacement (i.e., the lower is the capacity, the lower is the yielding displacement), this does not hold always true in terms of ultimate displacement. This is especially evident for the scenario 0p, where the local rebars buckling is prevented for the scenario 0p after about 65 years, thereby causing a temporary significant increment of the ultimate displacement with respect to the sound RC bridge column. Once a global buckling mode takes place, however, the ultimate displacement becomes less than the corresponding value for the sound RC bridge column also for the scenario 0p. It can also be observed that the corrosion has more influence on the yielding displacement rather than on the ultimate displacement

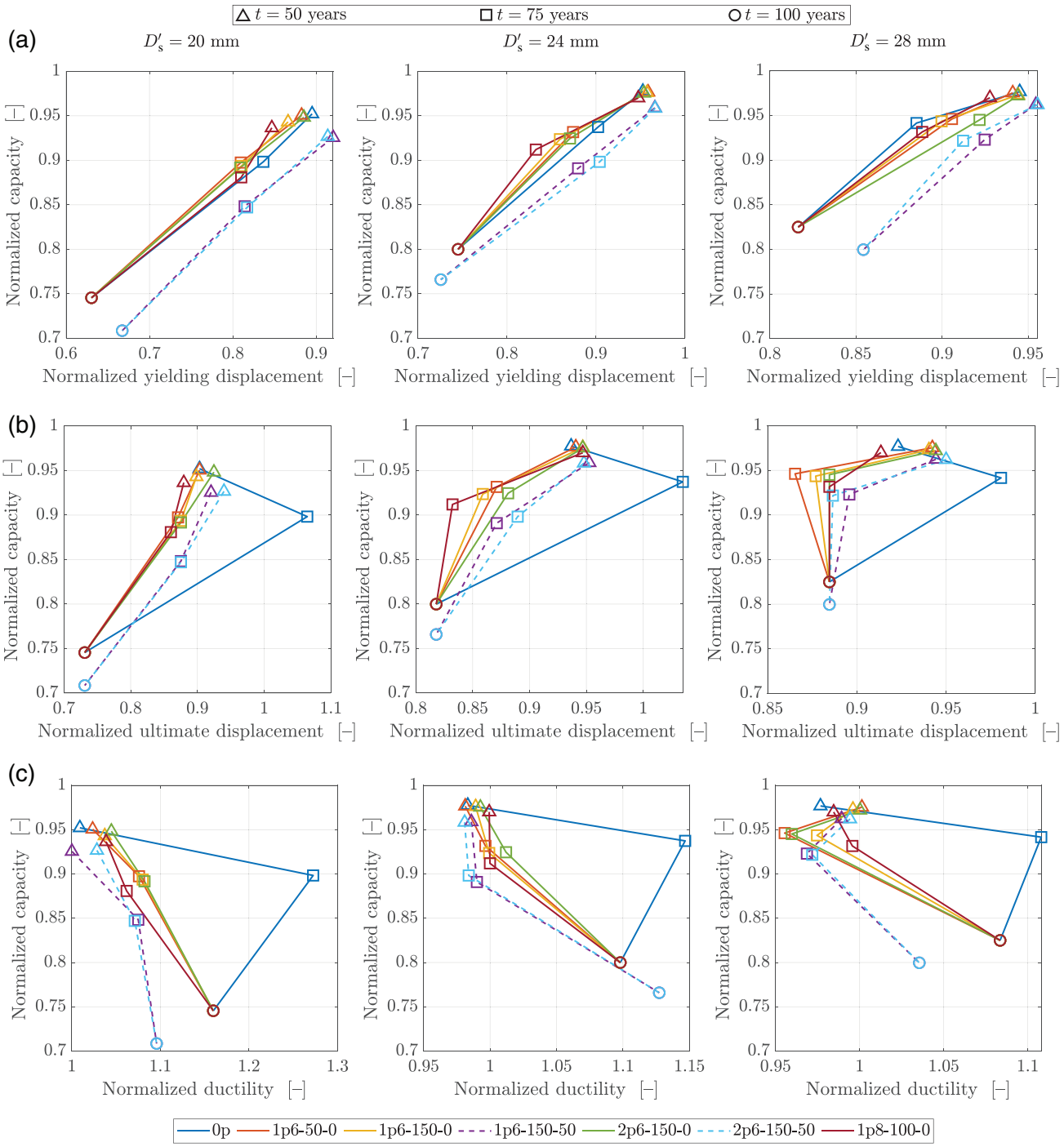

FIGURE 17 Yielding displacement (up), ultimate displacement (center), and ductility (down) normalized with respect to the corresponding values for the uncorroded RC bridge column at $t = \{50, 75, 100\}$ years considering $D'_s = \{20, 24, 28\}$ mm

(i.e., yielding displacement degrades with time faster than ultimate displacement). Once the global buckling mode of the longitudinal rebars is triggered, the geometrical features of the pits do not matter whereas the simultaneous presence of the generalized corrosion can have a moderate influence.

Overall, Figure 17 confirms that additional intermediate pits in the longitudinal rebar less severe than that of the two pits at the level of the transverse reinforcement do not affect significantly the considered RC bridge column behavior, regardless of their number or length (i.e., normalized curves for scenarios 1p6-50-0, 1p6-150-0, and 2p6-150-0 are very close to each other). The occurrence of a generalized corrosion in the longitudinal rebar has moderate influence on the column capacity only, regardless of the number of pits already in place (i.e., normalized

TABLE 3 Capacity and displacement ductility values for the uncorroded RC bridge column

	Uncorroded RC bridge column	
D'_s [mm]	Capacity [kN]	Displacement ductility [−]
20	679.46	1.86
24	674.84	1.97
28	685.60	2.00

curves for scenarios 1p6-150-50 and 2p6-150-50 are very close each other). These scenarios markedly differ from those in which no pitting corrosion occurs in the longitudinal rebars in the middle of the spiral pitch, or an additional pit identical to that at the level of the transverse reinforcement takes place (i.e., normalized curves for scenarios 0p and, to a lesser extent, 1p8-100-0 are different from the others). The maximum tensile strain achieved in the present case study for the most stressed steel fiber is about 1.5% at the failure (where the failure corresponds to a force reduction equal to 20% with respect to the maximum value). Therefore, the estimated maximum tensile strain in the corroded longitudinal rebars is lower than the ultimate tensile strain evaluated according to Equation (30), and the failure is always due to concrete crushing.

5 | CONCLUSIONS

The present work has presented a comprehensive numerical methodology to predict the effects of chlorides-induced corrosion on RC bridge columns. The overall framework results rather articulated as it combines multiphysics simulations and nonlinear structural analyses. This level of complexity is motivated by the need of forecasting the time-dependent cyclic behavior of the RC bridge columns with a satisfactory level of accuracy. The main findings of the present work can be summarized as follows.

- Multiphysics analyses for long-term performance assessment of RC bridges under corrosion require a large computational effort, but some simplifications might be introduced to reduce the total elaboration time. Herein, physics-based models have been employed to simulate the effects of environmental factors and aging whereas available data-driven models have been considered to take into account the effect of concrete cover cracking due to rebars corrosion in such a way to avoid time-consuming nonlinear static analyses.
- A convenient way to parameterize the corrosion pattern in terms of both localized and generalized corrosion has been here adopted. This facilitates a rational assessment of the RC bridges for different corrosion scenarios. In this regard, the case study here investigated has shown that the flexural behavior of RC bridge columns is mostly governed by localized corrosion. The generalized corrosion has moderate influence on the capacity, and its impact is even smaller in terms of ductility.
- It has been highlighted that the behavior of bare bars under pitting corrosion is strongly affected by the corrosion pattern. Under compression, pit length and number of pits as well as the simultaneous occurrence of the generalized corrosion do not have as much impact as the pits arrangement. Conversely, these parameters have greater influence under tension.
- The numerical results for bare bars under compression have shown that post-yield buckling might be prevented as the corrosion progresses. This, in turn, can change drastically the cyclic behavior of RC bridge columns over time. Experimental investigations are required to validate this numerical prediction. Generally, the occurrence, or otherwise, of local buckling as well as the onset of global buckling of the longitudinal rebars complicates the time-dependent prediction of the cyclic response of RC bridge columns. However, once the global buckling of longitudinal rebars is triggered, the corrosion pattern has no influence, with the only exception of the minor role played by the generalized corrosion. As this typically takes place after a long time, it brings down the impact of the large uncertainties inherent to long-term forecasting of exposure conditions.
- The considered RC bridge column was found very sensitive to the rebar response under compression while the ultimate strain was never attained under tension. Failure under tension might occur in different situations. In general, geometry of the RC bridge column cross-section and axial load level are expected to influence the failure conditions. Therefore, further parametric investigations should be directed toward understanding the role of cross-section geometry and axial load level in combination with the corrosion pattern on failure modes.

ACKNOWLEDGMENTS

It is acknowledged the support from the Laboratories University Network of Seismic Engineering (ReLUIS) through the research project DPC/ReLUIS 2019-2021—UR RM3 WP 11.2-11.3 (by Davide Lavorato, Camillo Nuti, and Angelo Pelle) and UR RM1 WP 4-11 (by Giuseppe Quaranta). The support from Federbeton (Italy) through the research project "Seismic Behavior of Integral Bridges" is acknowledged by Davide Lavorato, Camillo Nuti, and Angelo Pelle. Bruno Briseghella acknowledges the financial support from the National Natural Science Foundation of China (Grant No. 51778148). The work by Giuseppe Quaranta is framed within the research project "Smart technologies and

decision support tools for the assessment of deteriorating reinforced concrete infrastructures in seismic areas at territorial scale" (Grant No. RM120172B37F0628) funded by Sapienza Università di Roma. The authors are grateful to Eng. Marco Manai at the Provincia di Oristano for kindly supplying the design data of the examined bridge.

DATA AVAILABILITY STATEMENT

Further data that support the findings of this study are available from the corresponding author upon reasonable request.

ORCID

Angelo Pelle https://orcid.org/0000-0001-5842-7531
Bruno Briseghella https://orcid.org/0000-0002-8002-2298
Alessandro Vittorio Bergami https://orcid.org/0000-0002-7761-2190
Gabriele Fiorentino https://orcid.org/0000-0002-6444-0473
Davide Lavorato https://orcid.org/0000-0001-7753-1975
Giuseppe Quaranta https://orcid.org/0000-0001-8295-0912
Alessandro Rasulo https://orcid.org/0000-0003-4911-1812
Camillo Nuti https://orcid.org/0000-0002-0385-201X

REFERENCES

1. Val D. Deterioration of strength of RC beams due to corrosion and its influence on beam reliability. J Struct Eng. 2007;133(9):1297–306.
2. Marano GC, Quaranta G, Mezzina M. Fuzzy time-dependent reliability analysis of RC beams subject to pitting corrosion. J Mater Civ Eng. 2008;20(9):578–87.
3. Alogdianakis F, Charmpis DC, Balafas I. Macroscopic effect of distance from seacoast on bridge deterioration–statistical data assessment of structural condition recordings. Structure. 2020;27:319–29.
4. Wang X, Stewart MG, Nguyen M. Impact of climate change on corrosion and damage to concrete infrastructure in Australia. Clim Change. 2012;110(3):941–57.
5. Alipour A, Shafei B, Shinozuka M. Performance evaluation of deteriorating highway bridges located in high seismic areas. J Bridge Eng. 2011;16(5):597–611.
6. Alipour A, Shafei B, Shinozuka M. Capacity loss evaluation of reinforced concrete bridges located in extreme chloride-laden environments. Struct Infrastruct Eng. 2013;9(1):8–27.
7. Zhou X, Tu X, Chen A, Wang Y. Numerical simulation approach for structural capacity of corroded reinforced concrete bridge. Adv Concr Constr. 2019;7(1):11.
8. Kashani MM, Lowes LN, Crewe AJ, Alexander NA. Phenomenological hysteretic model for corroded reinforcing bars including inelastic buckling and low-cycle fatigue degradation. Comput Struct. 2015;156:58–71.
9. Kashani MM, Lowes LN, Crewe AJ, Alexander NA. Nonlinear fibre element modelling of RC bridge piers considering inelastic buckling of reinforcement. Eng Struct. 2016;116:163–77.
10. Rasulo A, Pelle A, Lavorato D, Fiorentino G, Nuti C, Briseghella B. Finite element analysis of reinforced concrete bridge piers including a flexure-shear interaction model. Appl Sci. 2020;10(7):2209.
11. Conti E, Malerba PG, Quagliaroli M, Scaperrotta D. Residual capacity of a reinforced concrete grillage deck exposed to corrosion. Struct Infrastruct Eng. 2020;16(1):202–18.
12. Marí A, Bairán J-M, Oller E, Duarte N. Modeling serviceability performance and ultimate capacity of corroded reinforced and prestressed concrete structures. Struct Concr. (2021, in press).
13. Kashani MM, Maddocks J, Dizaj EA. Residual capacity of corroded reinforced concrete bridge components: state-of-the-art review. J Bridge Eng. 2019;24(7):03119001.
14. Belletti B, Rodríguez J, Andrade C, Franceschini L, Sanchez MJ, Vecchi F. Experimental tests on shear capacity of naturally corroded prestressed beams. Struct Concr. 2020;21(5):1777–93.
15. Belletti B, Vecchi F, Bandini C, Andrade C, Montero JS. Numerical evaluation of the corrosion effects in prestressed concrete beams without shear reinforcement. Struct Concr. 2020;21(5):1794–809.
16. Vereecken E, Botte W, Lombaert G, Caspeele R. Assessment of corroded prestressed and posttensioned concrete structures: a review. Struct Concr. (2021, in press).
17. Shafei B, Alipour A, Shinozuka M. Prediction of corrosion initiation in reinforced concrete members subjected to environmental stressors: a finiteelement framework. Cem Concr Res. 2012;42(2):365–76.
18. Muthulingam S, Rao BN. Non-uniform time-to-corrosion initiation in steel reinforced concrete under chloride environment. Corros Sci. 2014;82:304–15.
19. Shafei B, Alipour A, Shinozuka M. A stochastic computational framework to investigate the initial stage of corrosion in reinforced concrete superstructures. Comput Aided Civ Inf Eng. 2013;28(7):482–94.
20. Kwon SJ, Na UJ, Park SS, Jung SH. Service life prediction of concrete wharves with early-aged crack: probabilistic approach for chloride diffusion. Struct Saf. 2009;31(1):75–83.
21. Shao-feng Z, Chun-hua L, Rong-gui L. Experimental determination of chloride penetration in cracked concrete beams. Procedia Eng. 2011;24:380–4.
22. Pang Y, Wei K, Yuan W. Life-cycle seismic resilience assessment of highway bridges with fiberreinforced concrete piers in the corrosive environment. Eng Struct. 2020;222:111120.
23. Vidal T, Castel A, François R. Analyzing crack width to predict corrosion in reinforced concrete. Cem Concr Res. 2004;34(1):165–74.
24. Marano GC, Quaranta G, Sgobba S, Greco R, Mezzina M. Fuzzy reliability analysis of RC structures by using an improved time-dependent model of chloride ingress. Struct Infrastruct Eng. 2010;6(1–2):205–23.
25. Bažant ZP, Najjar LJ. Drying of concrete as a nonlinear diffusion problem. Cem Concr Res. 1971;1(5):461–73.
26. Bažant ZP, Najjar LJ. Nonlinear water diffusion in nonsaturated concrete. Matér Constr. 1972;5(1):3–20.
27. Saetta AV, Scotta RV, Vitaliani RV. Analysis of chloride diffusion into partially saturated concrete. Materials. 1993;90(5):441–51.
28. Liu T, Weyers RW. Modeling the dynamic corrosion process in chloride contaminated concrete structures. Cem Concr Res. 1998;28(3):365–79.
29. Liu Y. Modeling the time-to corrosion cracking of the cover concrete in chloride contaminated reinforced concrete structures. PhD thesis, Virginia Tech, 1996.

30. Zhang R, Castel A, François R. The corrosion pattern of reinforcement and its influence on serviceability of reinforced concrete members in chloride environment. Cem Concr Res. 2009; 39(11):1077–86.
31. Chen E, Berrocal CG, Löfgren I, Lundgren K. Correlation between concrete cracks and corrosion characteristics of steel reinforcement in pre-cracked plain and fibre-reinforced concrete beams. Mater Struct. 2020;53(2):1–22.
32. Zhu W, François R. Effect of corrosion pattern on the ductility of tensile reinforcement extracted from a 26-year-old corroded beam. Adv Concr Constr. 2013;1(2):121.
33. Val DV, Melchers RE. Reliability of deteriorating RC slab bridges. J Struct Eng. 1997;123(12):1638–44.
34. Cairns J, Plizzari GA, Du Y, Law DW, Franzoni C. Mechanical properties of corrosion-damaged reinforcement. ACI Mater J. 2005;102(4):256.
35. Dodd LL, Restrepo-Posada JI. Model for predicting cyclic behavior of reinforcing steel. J Struct Eng. 1995;121(3): 433–45.
36. Chen E, Berrocal CG, Fernandez I, Löfgren I, Lundgren K. Assessment of the mechanical behaviour of reinforcement bars with localised pitting corrosion by digital image correlation. Eng Struct. 2020;219:110936.
37. Zhu W, Francois R. Experimental investigation of the relationships between residual cross-section shapes and the ductility of corroded bars. Construct Build Mater. 2014;69:335–45.
38. Fernandez I, Bairán JM, Marí AR. Mechanical model to evaluate steel reinforcement corrosion effects on $\sigma-\epsilon$ and fatigue curves. Experimental calibration and validation. Eng Struct. 2016;118:320–33.
39. Apostolopoulos CA. The influence of corrosion and cross-section diameter on the mechanical properties of B500C steel. J Mater Eng Perform. 2009;18(2):190–5.
40. Kashani MM, Lowes LN, Crewe AJ, Alexander NA. Finite element investigation of the influence of corrosion pattern on inelastic buckling and cyclic response of corroded reinforcing bars. Eng Struct. 2014;75:113–25.
41. Dhakal RP, Maekawa K. Modeling for postyield buckling of reinforcement. J Struct Eng. 2002;128(9):1139–47.
42. Menegotto M, Pinto PE. Method of analysis for cyclically loaded RC plane frames including changes in geometry and non-elastic behavior of elements under combined normal force and bending. *Proc. of IABSE symposium on resistance and ultimate deformability of structures acted on by well defined repeated loads*. 1973;13:15–22.
43. Massone LM, López EE. Modeling of reinforcement global buckling in RC elements. Eng Struct. 2014;59:484–94.
44. Spacone E, Filippou FC, Taucer FF. Fibre beam–column model for non-linear analysis of R/C frames: part I. Formulation. Earthq Eng Struct Dyn. 1996;25(7):711–25.
45. Spacone E, Filippou FC, Taucer FF. Fibre beam–column model for non-linear analysis of R/C frames: part II. Applications. Earthq Eng Struct Dyn. 1996;25(7):727–42.
46. Coleman J, Spacone E. Localization issues in forcebased frame elements. J Struct Eng. 2001;127(11):1257–65.
47. Berry MP, Eberhard MO. Performance modeling strategies for modern reinforced concrete bridge columns. PEER Report 2007/07: Pacific Earthquake Engineering Research Center; 2006.
48. Zhao J, Sritharan S. Modeling of strain penetration effects in fiber-based analysis of reinforced concrete structures. ACI Mater J. 2007;104(2):133.
49. Kent DC, Park R. Flexural members with confined concrete. J Struct Div. 1971;97(7):1969–90.
50. Scott BD, Park R, Priestley MJN. Stress-strain behavior of concrete confined by overlapping hoops at low and high strain rates. ACI J Proc. 1982;79(1):13–27.
51. Coronelli D, Gambarova P. Structural assessment of corroded reinforced concrete beams: modeling guidelines. J Struct Eng. 2004;130(8):1214–24.
52. Dizaj EA, Madandoust R, Kashani MM. Exploring the impact of chloride-induced corrosion on seismic damage limit states and residual capacity of reinforced concrete structures. Struct Infrastruct Eng. 2018;14(6):714–29.
53. Popovics S. A numerical approach to the complete stress-strain curve of concrete. Cem Concr Res. 1973;3(5):583–99.
54. Mander JB, Priestley MJN, Park R. Theoretical stress-strain model for confined concrete. J Struct Eng. 1988;114(8):1804–26.
55. Monti G, Nuti C. Nonlinear cyclic behavior of reinforcing bars including buckling. J Struct Eng. 1992;118(12):3268–84.
56. Zhou Z, Nuti C, Lavorato D. Modeling of the mechanical behavior of stainless reinforcing steel. *Proc. of 10th fib International PhD Symposium in Civil Engineering*. 2014;515–520.
57. Zhou Z. Uniaxial material model for reinforcing bar including buckling in RC structures. PhD thesis, Roma Tre University, 2015.
58. 3.2 Task Group. *Modelling of structural perfomance of existing concrete structures 2020*. fib Bulletin: The International Federation for Structural Concrete; in press.
59. Lavorato D, Fiorentino G, Pelle A, Rasulo A, Bergami AV, Briseghella B, et al. A corrosion model for the interpretation of cyclic behavior of reinforced concrete sections. Struct Concr. 2020;21(5):1732–46.
60. Dhakal RP, Maekawa K. Reinforcement stability and fracture of cover concrete in reinforced concrete members. J Struct Eng. 2002;128(10):1253–62.
61. Kashani MM, Lowes LN, Crewe AJ, Alexander NA. Computational modelling strategies for nonlinear response prediction of corroded circular RC bridge piers. Adv Mater Sci Eng. 2016; 2016:2738265.
62. Pantazopoulou SJ. Detailing for reinforcement stability in RC members. J Struct Eng. 1998;124(6):623–32.
63. Apostolopoulos CA, Diamantogiannis G, Apostolopoulos AC. Assessment of the mechanical behavior in dual-phase steel B 400 C, B 450 C, and B 500 B in a marine environment. J Mater Civ Eng. 2016;28(2):04015097.
64. Francois R, Arliguie G. Effect of microcracking and cracking on the development of corrosion in reinforced concrete members. Mag Concr Res. 1999;51(2):143–50.
65. Fernandez I, Bairán JM, Marí AR. Corrosion effects on the mechanical properties of reinforcing steel bars. Fatigue and $\sigma-\epsilon$ behavior. Construct Build Mater. 2015;101:772–83.
66. Kowalsky MJ, Priestley MJN. Improved analytical model for shear strength of circular reinforced concrete columns in seismic regions. ACI Struct J. 2000;97(3):388–96.
67. Gomes A, Appleton J. Nonlinear cyclic stressstrain relationship of reinforcing bars including buckling. Eng Struct. 1997; 19(10):822–6.

AUTHOR BIOGRAPHIES

Angelo Pelle, PhD Student, Department of Architecture, Roma Tre University, Largo G. B. Marzi 10, 00153, Roma, Italy. Email: angelo.pelle@uniroma3.it

Bruno Briseghella, Full Professor and Dean, College of Civil Engineering, Fuzhou University, 2 Xue Yuan Road, University Town, Fuzhou, Fujian 350108, PR China. Email: bruno@fzu.edu.cn

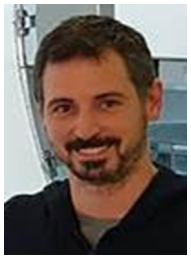

Alessandro Vittorio Bergami, Department of Architecture, Roma Tre University, Largo G. B. Marzi 10, 00153, Roma, Italy. Email: alessandro.bergami@uniroma3.it

Gabriele Fiorentino, Marie Curie Research Fellow, Department of Civil Engineering, University of Bristol, Queen's Building, University Walk, Bristol BS8 1TR. Email: gabriele.fiorentino@bristol.ac.uk

Gian Felice Giaccu, Assistant Professor, Department of Architecture, Design and Urban Planning, University of Sassari, Palazzo del Pou Salit, Piazza Duomo 6, 07041 Alghero, Italy. Email: gigiaccu@uniss.it

Davide Lavorato, Associate Professor, Department of Architecture, Roma Tre University, Largo G. B. Marzi 10, 00153, Roma, Italy. Email: davide.lavorato@uniroma3.it

Giuseppe Quaranta, Associate Professor, Department of Structural and Geotechnical Engineering, Sapienza University of Rome, Via Eudossiana 18, 00184 Rome, Italy. Email: giuseppe.quaranta@uniroma1.it

Alessandro Rasulo, Assistant Professor, Department of Civil and Mechanical Engineering, University of Cassino and Southern Lazio, Via G. Di Biasio 43, 03043 Cassino, Italy. Email: a.rasulo@unicas.it

Camillo Nuti, Full Professor, Department of Architecture, Roma Tre University, Largo G. B. Marzi 10, 00153, Roma, Italy. Email: camillo.nuti@uniroma3.it

How to cite this article: Pelle A, Briseghella B, Bergami AV, Fiorentino G, Giaccu GF, Lavorato D, et al. Time-dependent cyclic behavior of reinforced concrete bridge columns under chlorides-induced corrosion and rebars buckling. Structural Concrete. 2021;1–23. https://doi.org/10.1002/suco.202100257